LLNL-JRNL-704612

High order accurate finite difference modeling of seismo-acoustic wave propagation in a moving atmosphere and a heterogeneous earth model coupled across a realistic topography

N. Anders Petersson and Bjorn Sjogreen

October 16, 2016; Revised March 31, 2017

Submitted to Journal of Scientific Computing

Disclaimer

High order accurate finite difference modeling of seismo-acoustic wave propagation in a moving atmosphere and a heterogeneous earth model coupled across a realistic topography

N. Anders Petersson[*]   Björn Sjögren[!]

October 16, 2016, Revised March 31, 2017

Abstract

We develop a numerical method for simultaneously simulating acoustic waves in a realistic moving atmosphere and seismic waves in a heterogeneous earth model, where the motions are coupled across a realistic topography. We model acoustic wave propagation by solving the linearized Euler equations of compressible fluid mechanics. The seismic waves are modeled by the elastic wave equation in a heterogeneous anisotropic material. The motion is coupled by imposing continuity of normal velocity and normal stresses across the topographic interface. Realistic topography is resolved on a curvilinear grid that follows the interface. The governing equations are discretized using high order accurate finite difference methods that satisfy the principle of summation by parts. We apply the energy method to derive the discrete interface conditions and to show that the coupled discretization is stable. The implementation is verified by numerical experiments, and we demonstrate a simulation of coupled wave propagation in a windy atmosphere and a realistic earth model with non-planar topography.

1 Introduction

The modeling of energetic events near the Earths surface require coupled physics for accurate simulation of observed motions and interpretation of signals. One example is the burst of a large bolide, which can generate strong infra-sound signals as well as significant seismic signals [10]. However, most current simulation methods ignore the seismo-acoustic coupling. Instead, seismic and acoustic phenomena are usually modeled separately; in seismic modeling the atmosphere is replaced by a free surface boundary conditions, and in acoustic modeling the interface with the solid earth is modeled by a soft or hard wall.

Seismic wave propagation in the solid earth can be modeled by solving the visco-elastic wave equation in first order formulation for the particle velocity and stresses [35], or in second order formulation for the particle displacement [34]. The starting point of our development is the summation by parts (SBP) finite difference methods for seismic wave propagation in second order formulation [18], [3], [23], [28], [24], [25], [27], as implemented in the open source code SW4 [26]. This code implements a 4th order accurate scheme to simulate seismic wave propagation in a heterogeneous visco-elastic material, and uses a curvilinear grid that conforms to the topography, allowing the free surface boundary condition to be imposed at the correct location.

A SBP finite difference approximation [13], [31], [16] is constructed such that any estimate for the partial differential equation (PDE) that is based on integration by parts, can also be carried out for the finite difference approximation. An important example is conservation of mechanical energy. Partial integration for the PDE can be replaced by partial summation for the finite difference approximation, leading to a numerical solution that conserves a discrete approximation of the mechanical energy. The technique applies to curvilinear and Cartesian grids, and results in a stable discretization of the normal stress boundary condition along the interface. The main objective of this paper is to generalize the SBP technique to the coupled solid-fluid configuration, leading to a new finite difference discretization that has the same strong numerical stability properties as our numerical method for the seismic wave equation.

---

[*] Center for Applied Scientific Computing, Lawrence Livermore National Laboratory, L-561, PO Box 808, Livermore CA 94551

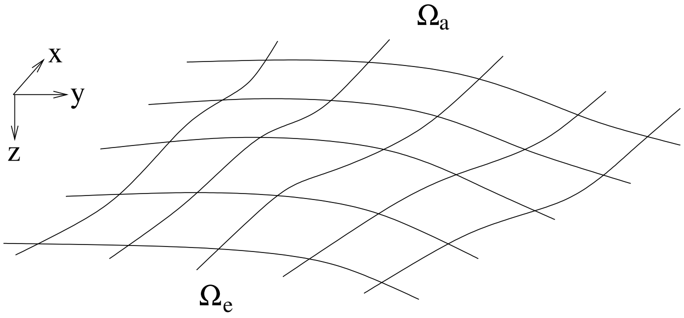

Figure 1: The topographic interface $x_3 = \tau(x_1,x_2)$ separates the acoustic domain (Ω_a) and the elastic domain (Ω_e).

We model acoustic wave propagation in a moving atmosphere by solving the linearized Euler equations of compressible fluid flow (see, e.g. Landau and Lifshitz [14], Ostashev et al. [21], or Munz et al. [17]). The acoustic waves are modeled as small perturbations on top of a given background pressure, velocity, and density field, which may vary in space and is assumed to be in balance with gravity. It is important to include effects of advection in the background flow field (i.e., wind), because it biases sound propagation in the direction of the wind and modifies the refraction of energy compared to a calm atmosphere (see, e.g. Arrowsmith et al., [4], or de Groot-Hedlin et al. [10]).

If the acoustic domain is considered in isolation, previous SBP techniques carry over to a finite difference method for the linearized Euler equations. However, finding stable discrete coupling conditions between the elastic and acoustic domains is less straightforward. The key is the derivation of appropriate coupling conditions between the elastic and acoustic sub-domains, and how to impose them during the time-stepping. In this paper we develop energy stable conditions that couple two finite difference discretizations of two different partial differential equations. With the proposed capability we are able to model energetic sources and the subsequent propagation of motions in the solid earth and the atmosphere, including the exchange of energy between both media. We formulate the governing equations in curvilinear coordinates and discretize them using finite differences that satisfy the SBP property. This leads to discrete interface conditions that make the coupled finite difference approximation energy stable. This approach generalizes our one-dimensional model of coupled elastic-acoustic wave propagation [29], and shares similarities with our previous technique for coupling two elastic wave equations on grids with hanging nodes along an interface [23].

The paper is organized as follows. The governing equations are presented in Section 2, where we also formulate the linearized Euler equations as a symmetric hyperbolic system. An energy estimate for the coupled problem is developed in Section 3. To handle non-planar topographic interfaces, we formulate the governing equations in curvilinear coordinates. This is done in Section 4, where we also generalize the energy estimate to the curvilinear formulation. The SBP discretization and the discretized interface conditions are presented in Section 5. We use the classical explicit fourth order Runge-Kutta method to integrate the coupled equations in time. Section 6 describes our discretization in time and how the interface conditions are enforced during the time-stepping. Numerical examples are presented in Section 7, followed by concluding remarks in Section 8.

2 Governing equations

We start by considering the whole-space domain where the atmosphere is separated from the solid earth along a topographic interface, which we assume to be described by the surface $x_3 = \tau(x_1,x_2)$, where $\mathbf{x} = (x_1,x_2,x_3)^T$ are the Cartesian coordinates. In this way the atmosphere and the solid earth occupy the sub-domains

$$\Omega_a = \{-\infty < x_3 \le \tau(x_1,x_2),\ \ -\infty < x_1 < \infty,\ \ -\infty < x_2 < \infty\}, \tag{1}$$

$$\Omega_e = \{\tau(x_1,x_2) \le x_3 < \infty,\quad -\infty < x_1 < \infty,\ \ -\infty < x_2 < \infty\}, \tag{2}$$

respectively. The two domains meet at the topographic interface $\Gamma = \Omega_a \cap \Omega_e$, where the outward unit normals are $\mathbf{n}_a$ and $\mathbf{n}_e = -\mathbf{n}_a$, respectively.

We model acoustic wave propagation in a moving heterogeneous atmosphere, governed by the compressible Euler equations for an ideal and perfect gas, linearized around a background flow field (density, velocity, pressure), denoted by $(\hat{\rho}(\mathbf{x}), \hat{\mathbf{u}}(\mathbf{x}), \hat{p}(\mathbf{x}))$. The background flow is assumed to satisfy the steady compressible Euler equations and to be in balance with gravity. The speed of sound satisfies $\hat{c} = \sqrt{\gamma\hat{p}/\hat{\rho}}$, where $\gamma > 1$ is the ratio of specific heats. The background flow is assumed sub-sonic, i.e., $|\hat{\mathbf{u}}| \ll \hat{c}$. Since there can not be any flow through the topographic interface, the background velocity can not have any normal component at the interface,

$$\mathbf{n}_a \cdot \hat{\mathbf{u}} = 0, \quad \mathbf{x} \in \Gamma. \tag{3}$$

The acoustic perturbations are denoted $(\rho, \mathbf{u}, p)^T$, where the components of the velocity perturbation are $\mathbf{u} = (u_1, u_2, u_3)^T$. The perturbations are assumed small, leading to the linearized compressible Euler system in primitive variables,

$$\rho_t + (\hat{\mathbf{u}} \cdot \nabla)\rho + (\mathbf{u} \cdot \nabla)\hat{\rho} + \hat{\rho}\nabla \cdot \mathbf{u} + \rho\nabla \cdot \hat{\mathbf{u}} = f_\rho, \tag{4}$$

$$\mathbf{u}_t + (\hat{\mathbf{u}} \cdot \nabla)\mathbf{u} + (\mathbf{u} \cdot \nabla)\hat{\mathbf{u}} + \frac{1}{\hat{\rho}}\nabla p - \frac{\rho}{\hat{\rho}^2}\nabla\hat{p} = \mathbf{f}_\mathbf{u}, \quad \mathbf{x} \in \Omega_a,\ t > 0, \tag{5}$$

$$p_t + (\hat{\mathbf{u}} \cdot \nabla)p + (\mathbf{u} \cdot \nabla)\hat{p} + \gamma\hat{p}\nabla \cdot \mathbf{u} + \gamma p\nabla \cdot \hat{\mathbf{u}} = f_p. \tag{6}$$

The forcing functions $f_\rho(\mathbf{x},t)$, $\mathbf{f}_\mathbf{u}(\mathbf{x},t)$, and $f_p(\mathbf{x},t)$, can be used to model acoustic sources. Note that the density equation (4) decouples from the velocity and pressure equations if the background pressure is constant, i.e., $\nabla\hat{p} = 0$. In the following, we consider the general case where all three equations must be solved simultaneously, see Ostashev et al. [21] for further discussions on acoustic modeling.

We model wave propagation in the solid earth by the elastic wave equation in second order differential form.

$$\rho_e \mathbf{w}_{tt} = \nabla \cdot \mathscr{T} + \mathbf{g}, \quad \mathbf{x} \in \Omega_e,\ t > 0, \tag{7}$$

$$\nabla \cdot \mathscr{T} = \mathbf{L}\mathbf{w}, \tag{8}$$

where $\mathbf{w}(\mathbf{x},t)$ is the displacement vector, $\mathbf{g}(\mathbf{x},t)$ is the external forcing, and $\rho_e(\mathbf{x}) > 0$ is the density. The divergence of the stress tensor equals the 3×3 symmetric Kelvin-Christoffel differential operator matrix [7], which is denoted $\mathbf{L}\mathbf{w}$. To easily handle anisotropic materials and curvilinear coordinates, we adopt the formulation developed in Petersson and Sjogreen [27] and write the spatial operator as

$$\mathbf{L}\mathbf{w} := \sum_{j=1}^{3} \partial_j \left(L_j \nabla \mathbf{w}\right), \quad L_j \nabla \mathbf{w} = \sum_{k=1}^{3} M^{jk} \partial_k \mathbf{w}. \tag{9}$$

Here, partial differentiation with respect to the Cartesian coordinates is denoted by $\partial_k = \partial/\partial x_k$. We consider general heterogeneous materials where $M^{jk} = M^{jk}(\mathbf{x})$. Each of the 3×3 matrices M^{jk} contain a subset of elements of the 6×6 stiffness matrix $\mathscr{C} = \mathscr{C}^T > 0$, which expresses Hooke's law in Voigt vector notation as $\sigma = \mathscr{C}\mathbf{e}$, see [7] and [27] for details. From the symmetry and positive definiteness of $\mathscr{C}$ it follows that M^{kk} are also symmetric and positive definite. Furthermore, the symmetry of $\mathscr{C}$ implies that the off-diagonal matrices satisfy $M^{kj} = (M^{jk})^T$. Our formulation applies to the full spectrum of elastic materials, from general anisotropic models with 21 unique parameters, to isotropic models where the stiffness matrix only depends on the Lamé parameters (λ, μ).

The acoustic and elastic wave equations are coupled along the topographic interface by imposing continuity of normal stresses and normal velocities,

$$\begin{cases} -p\mathbf{n} = \mathscr{T} \cdot \mathbf{n}, \\ \mathbf{n} \cdot \mathbf{u} = \mathbf{n} \cdot \mathbf{w}_t, \end{cases} \qquad \mathbf{n} = \pm\mathbf{n}_a = \mp\mathbf{n}_e, \quad \mathbf{x} \in \Gamma,\ t > 0. \tag{10}$$

2.1 Symmetrizing the linearized Euler equations

To facilitate an energy estimate for the linearized Euler equations, we start by transforming them to symmetric form. This can be done in several ways [1]. Here we use an approach that generalizes to the linearized Navier-Stokes equations. We make the variable substitutions

$$s = \frac{1}{\sqrt{\gamma}}\frac{\hat{c}}{\hat{\rho}}\rho, \quad r = -\frac{1}{\sqrt{\gamma(\gamma-1)}}\frac{\hat{c}}{\hat{\rho}}\rho + \frac{\sqrt{\gamma}}{\sqrt{\gamma-1}}\frac{1}{\hat{\rho}\hat{c}}p, \tag{11}$$

which transforms (4)-(6) to a symmetric hyperbolic system for the dependent variable $\mathbf{q} = (s, u_1, u_2, u_3, r)^T$,

$$\mathbf{q}_t + A\partial_1\mathbf{q} + B\partial_2\mathbf{q} + C\partial_3\mathbf{q} + E\mathbf{q} = \mathbf{f}, \quad \mathbf{x} \in \Omega_a, \;\; t > 0, \tag{12}$$

Here, $\mathbf{f} = \mathbf{f}(\mathbf{x}, t)$ represents the external forcing. The matrices A, B satisfy

$$A = \begin{pmatrix} \hat{u}_1 & \frac{1}{\sqrt{\gamma}}\hat{c} & 0 & 0 & 0 \\ \frac{1}{\sqrt{\gamma}}\hat{c} & \hat{u}_1 & 0 & 0 & \sqrt{\frac{\gamma-1}{\gamma}}\hat{c} \\ 0 & 0 & \hat{u}_1 & 0 & 0 \\ 0 & 0 & 0 & \hat{u}_1 & 0 \\ 0 & \sqrt{\frac{\gamma-1}{\gamma}}\hat{c} & 0 & 0 & \hat{u}_1 \end{pmatrix}, \quad B = \begin{pmatrix} \hat{u}_2 & 0 & \frac{1}{\sqrt{\gamma}}\hat{c} & 0 & 0 \\ 0 & \hat{u}_2 & 0 & 0 & 0 \\ \frac{1}{\sqrt{\gamma}}\hat{c} & 0 & \hat{u}_2 & 0 & \sqrt{\frac{\gamma-1}{\gamma}}\hat{c} \\ 0 & 0 & 0 & \hat{u}_2 & 0 \\ 0 & 0 & \sqrt{\frac{\gamma-1}{\gamma}}\hat{c} & 0 & \hat{u}_2 \end{pmatrix}, \tag{13}$$

and the matrix C is given by

$$C = \begin{pmatrix} \hat{u}_3 & 0 & 0 & \frac{1}{\sqrt{\gamma}}\hat{c} & 0 \\ 0 & \hat{u}_3 & 0 & 0 & 0 \\ 0 & 0 & \hat{u}_3 & 0 & 0 \\ \frac{1}{\sqrt{\gamma}}\hat{c} & 0 & 0 & \hat{u}_3 & \sqrt{\frac{\gamma-1}{\gamma}}\hat{c} \\ 0 & 0 & 0 & \sqrt{\frac{\gamma-1}{\gamma}}\hat{c} & \hat{u}_3 \end{pmatrix}. \tag{14}$$

The matrix of the zeroth order term is given by

$$E = \begin{pmatrix} \nabla\cdot\hat{\mathbf{u}} - \frac{3}{\hat{c}}\hat{\mathbf{u}}\cdot\nabla\hat{c} + \frac{1}{\hat{p}}\hat{\mathbf{u}}\cdot\nabla\hat{p} & \frac{\hat{c}}{\hat{p}\sqrt{\gamma}}(\nabla\hat{p})^T - \frac{2}{\sqrt{\gamma}}(\nabla\hat{c})^T & 0 \\ -\frac{1}{\sqrt{\gamma}}\nabla\hat{c} & \nabla\hat{\mathbf{u}} & \sqrt{\frac{\gamma-1}{\gamma}}\left(\frac{\hat{c}}{\hat{p}}\nabla\hat{p} - \nabla\hat{c}\right) \\ \sqrt{\gamma-1}\,\nabla\cdot\hat{\mathbf{u}} + \frac{2}{\hat{c}\sqrt{\gamma-1}}\hat{\mathbf{u}}\cdot\nabla\hat{c} & \frac{2}{\sqrt{\gamma(\gamma-1)}}(\nabla\hat{c})^T & \gamma\nabla\cdot\hat{\mathbf{u}} - \frac{1}{\hat{c}}\hat{\mathbf{u}}\cdot\nabla\hat{c} + \frac{1}{\hat{p}}\hat{\mathbf{u}}\cdot\nabla\hat{p} \end{pmatrix}.$$

Note that A, B, and C are symmetric for all heterogeneous background fields. The matrix E is zero when the background flow field is constant.

3 Energy estimates

In this section we derive an energy estimate for the continuous problem. This estimate shows what interface condition must be enforced along Γ to control the rate of total energy in the coupled elastic-acoustic system.

3.1 The linearized Euler equations

Because the background flow field may vary in space, the matrices A, B, and C in (12) will in general also depend on $\mathbf{x}$. To obtain an energy estimate, we therefore need to write the symmetrized linearized Euler system (12) on split form. Moreover, to obtain a boundary term that matches the interface condition (10), we scale the split form by the density, e.g.,

$$A\partial_1\mathbf{q} = \frac{1}{2}A\partial_1\mathbf{q} + \frac{1}{2\hat{\rho}}\partial_1(\hat{\rho}A\mathbf{q}) - \frac{1}{2\hat{\rho}}\partial_1(\hat{\rho}A)\mathbf{q},$$

and similarly for $B\partial_2\mathbf{q}$ and $C\partial_3\mathbf{q}$. Equation (12) becomes

$$\mathbf{q}_t + \frac{1}{2}\left[A\partial_1\mathbf{q} + B\partial_2\mathbf{q} + C\partial_3\mathbf{q}\right] + \frac{1}{2\hat{\rho}}\left[\partial_1(\hat{\rho}A\mathbf{q}) + \partial_2(\hat{\rho}B\mathbf{q}) + \partial_3(\hat{\rho}C\mathbf{q})\right] + H\mathbf{q} = \mathbf{f}. \tag{15}$$

We call this system the symmetrized linearized Euler equations in density scaled split form. The matrix of the zeroth order term now satisfies

$$H = E - \frac{1}{2\hat{\rho}}\left(\partial_1(\hat{\rho}A) + \partial_2(\hat{\rho}B) + \partial_3(\hat{\rho}C)\right).$$

A norm estimate for solutions of the symmetrized linearized Euler equations in density scaled split form (15) can be obtained by forming[1]

$$\frac{1}{2}\frac{d}{dt}(\hat{\rho}\mathbf{q},\mathbf{q})_{\Omega_a} = (\hat{\rho}\mathbf{q},\mathbf{q}_t)_{\Omega_a} = -\frac{1}{2}(\hat{\rho}\mathbf{q},A\partial_1\mathbf{q})_{\Omega_a} - \frac{1}{2}(\hat{\rho}\mathbf{q},B\partial_2\mathbf{q})_{\Omega_a} - \frac{1}{2}(\hat{\rho}\mathbf{q},C\partial_3\mathbf{q})_{\Omega_a}$$
$$-\frac{1}{2}(\mathbf{q},\partial_1(\hat{\rho}A\mathbf{q}))_{\Omega_a} - \frac{1}{2}(\mathbf{q},\partial_2(\hat{\rho}B\mathbf{q}))_{\Omega_a} - \frac{1}{2}(\mathbf{q},\partial_3(\hat{\rho}C\mathbf{q}))_{\Omega_a} - (\hat{\rho}\mathbf{q},H\mathbf{q})_{\Omega_a} + (\hat{\rho}\mathbf{q},\mathbf{f})_{\Omega_a}. \quad (16)$$

By Gauss theorem and the symmetry of the matrices A, B, and C, we arrive at

$$\frac{1}{2}\frac{d}{dt}(\hat{\rho}\mathbf{q},\mathbf{q})_{\Omega_a} = -\frac{1}{2}\int_{\Gamma}\hat{\rho}\mathbf{q}\cdot\widehat{A}\mathbf{q}\,d\Gamma - (\hat{\rho}\mathbf{q},H\mathbf{q})_{\Omega_a} + (\hat{\rho}\mathbf{q},\mathbf{f})_{\Omega_a}, \quad (17)$$

where

$$\widehat{A} = n_1A + n_2B + n_3C, \quad \mathbf{n}_a = (n_1,n_2,n_3)^T, \quad \mathbf{x}\in\Gamma. \quad (18)$$

Because of condition (3), the normal component of the background velocity field is zero along the interface. After some algebra we obtain,

$$\hat{\rho}\mathbf{q}\cdot\widehat{A}\mathbf{q} = 2p(\mathbf{n}_a\cdot\mathbf{u}), \quad \mathbf{x}\in\Gamma.$$

Hence, if the linearized Euler equations are solved independently of the elastic wave equation, the boundary term in (17) cancels if either $\mathbf{n}_a\cdot\mathbf{u} = 0$, or $p = 0$, along the boundary. These boundary conditions correspond to hard and soft wall conditions in acoustic modeling.

To gain physical understanding of the expression for the energy $(\hat{\rho}\mathbf{q},\mathbf{q})_{\Omega_a}$ in (17), we use (11) to express it in terms of the original variables,

$$(\hat{\rho}\mathbf{q},\mathbf{q})_{\Omega_a} = \int_{\Omega_a}\left\{\hat{\rho}(u^2+v^2+w^2) + \frac{\hat{c}^2\rho^2 - 2\rho p + p^2\gamma/\hat{c}^2}{\hat{\rho}(\gamma-1)}\right\}d\Omega. \quad (19)$$

The energy can be decomposed into its kinematic and potential components,

$$K = \int_{\Omega_a}\hat{\rho}(u^2+v^2+w^2)\,d\Omega, \quad P = \int_{\Omega_a}\frac{\hat{c}^2\rho^2 - 2\rho p + p^2\gamma/\hat{c}^2}{\hat{\rho}(\gamma-1)}\,d\Omega.$$

The potential component can be further decomposed as

$$P = P_1 + P_2, \quad P_1 = \int_{\Omega_a}\frac{p^2}{\hat{\rho}\hat{c}^2}\,d\Omega, \quad P_2 = \int_{\Omega_a}\frac{\hat{c}^2}{\hat{\rho}(\gamma-1)}\left(\rho - \frac{p}{\hat{c}^2}\right)^2 d\Omega, \quad (20)$$

where the speed of sound relation, $\hat{c} = \sqrt{\gamma\hat{p}/\hat{\rho}}$, was used to simplify the expressions. Here, P_1 is the acoustic potential energy. When the background pressure is in static equilibrium with gravity, the term P_2 equals the gravitational potential energy. It can be written

$$P_g = \int_{\Omega_a}\frac{g^2}{\hat{\rho}\mathcal{N}^2}\left(\rho - \frac{p}{\hat{c}^2}\right)^2 d\Omega, \quad \mathcal{N}^2 := -g\left(-\frac{1}{\hat{\rho}}\frac{d\hat{\rho}}{dx_3} + \frac{g}{\hat{c}^2}\right), \quad (21)$$

where $\mathcal{N}^2$ is the Brunt-Väisälä frequency, see Gill [9] and Appendix A for details.

3.2 The elastic wave equation

An energy estimate for the elastic wave equation (7) can be derived by integration by parts,

$$\frac{1}{2}\frac{d}{dt}(\mathbf{w}_t,\rho_e\mathbf{w}_t)_{\Omega_e} = (\mathbf{w}_t,\nabla\cdot\mathscr{T})_{\Omega_e} + (\mathbf{w}_t,\mathbf{g})_{\Omega_e}$$
$$= -(\nabla\mathbf{w}_t,\mathscr{T})_{\Omega_e} + \int_{\Gamma}\mathbf{w}_t\cdot(\mathscr{T}\cdot\mathbf{n}_e)\,d\Gamma + (\mathbf{w}_t,\mathbf{g})_{\Omega_e} \quad (22)$$

---

[1] The L_2 scalar product of real-valued vector functions on the domain $\mathbf{x}\in\Omega$ is defined by $(\mathbf{v},\mathbf{w})_{\Omega} = \int_{\Omega}\mathbf{v}\cdot\mathbf{w}\,d\Omega$. Here, $\mathbf{v}(\mathbf{x})$ and $\mathbf{w}(\mathbf{x})$ are assumed to decay as $|\mathbf{x}|\to\infty$, such that the integral is convergent.

From the definition of the stress tensor (8)-(9),

$$(\nabla \mathbf{w}_t, \mathscr{T})_{\Omega_e} = \int_{\Omega_e} \begin{pmatrix} \partial_1 \mathbf{w}_t^T & \partial_2 \mathbf{w}_t^T & \partial_3 \mathbf{w}_t^T \end{pmatrix} \begin{pmatrix} M^{11} & M^{12} & M^{13} \\ M^{21} & M^{22} & M^{23} \\ M^{31} & M^{32} & M^{33} \end{pmatrix} \begin{pmatrix} \partial_1 \mathbf{w} \\ \partial_2 \mathbf{w} \\ \partial_3 \mathbf{w} \end{pmatrix} d\Omega =: S(\mathbf{w}_t, \mathbf{w}). \tag{23}$$

The properties of the matrices M^{jk} imply that $S(\mathbf{v},\mathbf{w}) = S(\mathbf{w},\mathbf{v})$ and $S(\mathbf{w},\mathbf{w}) \geq 0$, see [27] for details. These properties lead to the energy estimate,

$$\frac{1}{2}\frac{d}{dt}\left[(\rho_e \mathbf{w}_t, \mathbf{w}_t)_{\Omega_e} + S(\mathbf{w},\mathbf{w})\right] = \int_\Gamma \mathbf{w}_t \cdot (\mathscr{T} \cdot \mathbf{n}_e)\, d\Gamma + (\mathbf{w}_t, \mathbf{g})_{\Omega_e}, \tag{24}$$

where the terms $(\rho_e \mathbf{w}_t, \mathbf{w}_t)_{\Omega_e}$ and $S(\mathbf{w},\mathbf{w})$ represent the kinematic and potential elastic energies, respectively. The null-space of S corresponds to solid body translations and rotations.

3.3 The coupled elastic-acoustic system

By combining the norm estimates (24) and (17) over the elastic and acoustic domains,

$$\begin{aligned} &\frac{1}{2}\frac{d}{dt}\left((\rho_e \mathbf{w}_t, \mathbf{w}_t)_{\Omega_e} + S(\mathbf{w},\mathbf{w}) + (\hat{\rho}\mathbf{q},\mathbf{q})_{\Omega_a}\right) \\ &\qquad = \int_\Gamma \mathbf{w}_t \cdot (\mathscr{T} \cdot \mathbf{n}_e)\, d\Gamma - \int_\Gamma p(\mathbf{n}_a \cdot \mathbf{u})\, d\Gamma - (\hat{\rho}\mathbf{q}, H\mathbf{q})_{\Omega_a} + (\mathbf{w}_t, \mathbf{g})_{\Omega_e} + (\hat{\rho}\mathbf{q}, \mathbf{f})_{\Omega_a}. \end{aligned} \tag{25}$$

Assuming that no energy is lost or generated along the interface, we require

$$\mathbf{w}_t \cdot (\mathscr{T} \cdot \mathbf{n}_e) - p(\mathbf{n}_a \cdot \mathbf{u}) = 0, \quad \mathbf{x} \in \Gamma. \tag{26}$$

Note that the outward normal from the acoustic domain equals the inward normal from the elastic domain, i.e., $\mathbf{n}_a = -\mathbf{n}_e$. Hence, (26) can be written $\mathbf{w}_t \cdot (\mathscr{T} \cdot \mathbf{n}_e) + p(\mathbf{n}_e \cdot \mathbf{u}) = 0$, which is satisfied if the interface conditions (10) are satisfied. As a result the two boundary terms in (25) cancel and we arrive at

$$\frac{1}{2}\frac{d}{dt}\Big((\rho_e \mathbf{w}_t, \mathbf{w}_t)_{\Omega_e} + S(\mathbf{w},\mathbf{w}) + (\hat{\rho}\mathbf{q},\mathbf{q})_{\Omega_a}\Big) = -(\hat{\rho}\mathbf{q}, H\mathbf{q})_{\Omega_a} + (\hat{\rho}\mathbf{q}, \mathbf{f})_{\Omega_a} + (\mathbf{w}_t, \mathbf{g})_{\Omega_e}. \tag{27}$$

Thus, the rate of total energy in the coupled elastic-acoustic model is not affected by the interface condition between the elastic and acoustic domains. The total energy in the system is conserved in the absence of external forcing and when the matrix $H = 0$, i.e., when the background flow field is constant. However, for a general background flow field, the matrix H can have positive or negative eigenvalues, leading to bounded decay or growth of the total energy.

4 Curvilinear coordinates

We use curvilinear coordinates to model non-planar topographic interfaces Γ. We start by developing a curvilinear formulation of the governing equations that satisfies an energy estimate. The steps in deriving the estimate serve as a guiding principle for developing a stable finite difference discretization based on the summation by parts (SBP) principle. In this approach, integrals are replaced by weighted sums, and integration by parts is replaced by corresponding summation by parts rules for boundary modified difference operators. As we will show in Section 5, this approach leads to a provably stable finite difference approximation of the coupled wave propagation problem, where the discretization of the interface condition (10) follows as a requirement for stability.

To introduce our notation we start by recalling some properties of curvilinear mappings, see [33] for details. We focus on the atmospheric domain Ω_a; the elastic domain Ω_e can be treated in a similar way. Assume that there is a one-to-one forward mapping function $\mathbf{x} = \mathbf{x}(\mathbf{r})$,

$$\mathbf{x}(\mathbf{r}) = (x_1(\mathbf{r}), x_2(\mathbf{r}), x_3(\mathbf{r}))^T, \quad \mathbf{r} = (r_1, r_2, r_3)^T,$$

from the half-space in parameter coordinates, $(r_1, r_2) \in (-\infty, \infty)^2$, $-\infty < r_3 \leq 0$, to the acoustic domain $\mathbf{x} \in \Omega_a$. The mapping is assumed non-singular and the inverse is formally $\mathbf{r} = \mathbf{r}(\mathbf{x})$. We denote partial differentiation with respect to the parameter coordinates by $\tilde{\partial}_k = \partial/\partial r_k$. By the chain rule,

$$\tilde{\partial}_q = \sum_{p=1}^{3} \frac{\partial x_p}{\partial r_q} \partial_p, \quad q = 1,2,3, \quad \partial_i = \sum_{j=1}^{3} \frac{\partial r_j}{\partial x_i} \tilde{\partial}_j, \quad i = 1,2,3. \tag{28}$$

The derivatives of the forward and inverse mapping functions define the covariant and contravariant base vectors,

$$\mathbf{a}_k := \tilde{\partial}_k \mathbf{x} = \begin{pmatrix} \partial x_1/\partial r_k \\ \partial x_2/\partial r_k \\ \partial x_3/\partial r_k \end{pmatrix}, \quad \mathbf{a}^k := \nabla r_k = \begin{pmatrix} \partial r_k/\partial x_1 \\ \partial r_k/\partial x_2 \\ \partial r_k/\partial x_3 \end{pmatrix}, \quad k = 1,2,3, \tag{29}$$

respectively. It is well-known (see [33] for details) that the contravariant base vectors can be expressed in terms of the covariant base vectors,

$$\mathbf{a}^i = \frac{1}{J} \left(\mathbf{a}_j \times \mathbf{a}_k \right), \quad (i,j,k) \text{ cyclic}, \quad J = \det\left(\mathbf{a}_1 \; \mathbf{a}_2 \; \mathbf{a}_3 \right). \tag{30}$$

This relation provides a convenient way of calculating the contravariant base vectors without explicitly knowing the inverse mapping function. Here, J is the Jacobian of the forward mapping function, which is assumed to satisfy $0 < J < \infty$.

By using the metric identity (see [33]),

$$\tilde{\partial}_1 (J\mathbf{a}^1) + \tilde{\partial}_2 (J\mathbf{a}^2) + \tilde{\partial}_3 (J\mathbf{a}^3) = 0,$$

we obtain the non-conservative and conservative forms of the gradient and divergence operators,

$$\nabla u = \frac{1}{J} \sum_{i=1}^{3} \left[J\mathbf{a}^i \tilde{\partial}_i u \right] = \frac{1}{J} \sum_{i=1}^{3} \tilde{\partial}_i \left[J\mathbf{a}^i u \right], \tag{31}$$

$$\nabla \cdot \mathbf{U} = \frac{1}{J} \sum_{i=1}^{3} \left[(J\mathbf{a}^i \cdot \tilde{\partial}_i \mathbf{U} \right] = \frac{1}{J} \sum_{i=1}^{3} \tilde{\partial}_i \left[J\mathbf{a}^i \cdot \mathbf{U} \right]. \tag{32}$$

In the last formula, $\mathbf{U}$ can be a tensor or a vector.

When the topographic interface can be described by $x_3 = \tau(x_1, x_2)$, the mapping for the acoustic domain can be constructed from the function τ. For example, by using a polynomial stretching in the vertical direction,

$$\begin{pmatrix} x_1(\mathbf{r}) \\ x_2(\mathbf{r}) \\ x_3(\mathbf{r}) \end{pmatrix} = \begin{pmatrix} r_1 \\ r_2 \\ Z(\mathbf{r}) \end{pmatrix}, \quad Z(\mathbf{r}) = \begin{cases} r_3, & r_3 < z_0, \\ r_3 + \left(1 - \frac{r_3}{z_0}\right)^m \tau(r_1, r_2), & z_0 \leq r_3 \leq 0. \end{cases}$$

Here, $z_0 \ll \min \tau$ is a constant and m is a natural number that controls the smoothness of the mapping at $r_3 = z_0$. A similar mapping for the elastic domain follows by trivial modifications.

4.1 The linearized Euler equations

The symmetrized linearized Euler system in density scaled split form (15) can be transformed to curvilinear coordinates by combining the conservative and non-conservative gradient and divergence operators (31)-(32). After some algebra,

$$\mathbf{q}_t + \frac{1}{2J} \left[\tilde{A} \tilde{\partial}_1 \mathbf{q} + \tilde{B} \tilde{\partial}_2 \mathbf{q} + \tilde{C} \tilde{\partial}_3 \mathbf{q} \right] + \frac{1}{2J\hat{\rho}} \left[\tilde{\partial}_1 (\hat{\rho} \tilde{A} \mathbf{q}) + \tilde{\partial}_2 (\hat{\rho} \tilde{B} \mathbf{q}) + \tilde{\partial}_3 (\hat{\rho} \tilde{C} \mathbf{q}) \right] + H\mathbf{q} = \mathbf{f}. \tag{33}$$

The elements of the transformed matrices can be expressed in terms of the components of the contravariant base vectors $\mathbf{a}^k = (\alpha_1^k, \alpha_2^k, \alpha_3^k)^T$,

$$\tilde{A}_{ij} = J\left(\alpha_1^1 A_{ij} + \alpha_2^1 B_{ij} + \alpha_3^1 C_{ij}\right), \tag{34}$$

$$\tilde{B}_{ij} = J\left(\alpha_1^2 A_{ij} + \alpha_2^2 B_{ij} + \alpha_3^2 C_{ij}\right), \tag{35}$$

$$\tilde{C}_{ij} = J\left(\alpha_1^3 A_{ij} + \alpha_2^3 B_{ij} + \alpha_3^3 C_{ij}\right). \tag{36}$$

Note that the symmetries of the matrices A, B, and C imply that also $\tilde{A}$, $\tilde{B}$, and $\tilde{C}$ are symmetric. Therefore, $k_1\tilde{A} + k_2\tilde{B} + k_3\tilde{C}$ has real eigenvalues for all real wave vectors $\mathbf{k} = (k_1, k_2, k_3)^T$. Hence, (33) is a symmetric hyperbolic system.

In curvilinear coordinates, the volume element in an integral is scaled by the Jacobian J, and the L_2 scalar product over Ω_a becomes

$$(\mathbf{u}, \mathbf{v})_{P_a} = \int_{r_1=-\infty}^{\infty} \int_{r_2=-\infty}^{\infty} \int_{r_3=-\infty}^{0} (\mathbf{u} \cdot \mathbf{v}) J\, dr_1\, dr_2\, dr_3. \tag{37}$$

An energy estimate can be derived in the same way as in the Cartesian case, because the factor J in the scalar product cancels the factors $1/J$ in front of the second and third terms in (33). After partial integration, we obtain an energy balance equation of the form (17), with boundary term

$$-\frac{1}{2} \iint \hat{\rho}\mathbf{q} \cdot \tilde{C}\mathbf{q}\Big|_{r_3=0} dr_1 dr_2. \tag{38}$$

We proceed by showing that (38) is equivalent to the boundary term on the right hand side of (17). In curvilinear coordinates the interface surface $\mathbf{x} \in \Gamma$ is parameterized by $\mathbf{x} = \mathbf{x}(r_1, r_2, 0)$ and corresponds to $r_3 = 0$ in parameter space. The outwards directed unit normal satisfies

$$\mathbf{n}_a = \frac{\nabla r_3}{|\nabla r_3|} = \frac{1}{|\mathbf{a}^3|} \begin{pmatrix} \alpha_1^3 \\ \alpha_2^3 \\ \alpha_3^3 \end{pmatrix}, \quad r_3 = 0.$$

Hence, by combining (36) and (18), $\tilde{C} = |\mathbf{a}^3| J\widehat{A}$. Furthermore, the surface element in (17) transforms according to $d\Gamma = \mathbf{n}_a \cdot (\mathbf{a}_1 \times \mathbf{a}_2)\, dr_1 dr_2 = |\mathbf{a}^3| J\, dr_1 dr_2$. Thus,

$$\iint \hat{\rho}\mathbf{q} \cdot \tilde{C}\mathbf{q}\Big|_{r_3=0} dr_1 dr_2 = \iint \hat{\rho}\mathbf{q} \cdot \widehat{A}\mathbf{q}\, |\mathbf{a}^3| J\Big|_{r_3=0} dr_1 dr_2 = \int_{\Gamma} \hat{\rho}\mathbf{q} \cdot \widehat{A}\mathbf{q}\, d\Gamma.$$

4.2 The elastic wave equation

Let the elastic domain correspond to the half-space $(r_1, r_2) \in (-\infty, \infty)^2$, $0 \le r_3 < \infty$ in parameter space, with the interface at $r_3 = 0$. For clarity we denote the Jacobian of the curvilinear mapping for the elastic domain by J_e, and the components of the contravariant base vectors by $\mathbf{b}^k = (\beta_1^k, \beta_2^k, \beta_3^k)^T$. Furthermore, the L_2 scalar product over the domain Ω_e becomes

$$(\mathbf{u}, \mathbf{v})_{P_e} = \int_{r_1=-\infty}^{\infty} \int_{r_2=-\infty}^{\infty} \int_{r_3=0}^{\infty} \mathbf{u} \cdot \mathbf{v} J_e\, dr_1\, dr_2\, dr_3. \tag{39}$$

In curvilinear coordinates, the spatial operator in the elastic wave equation (7) can be written

$$\mathbf{L}\mathbf{w} = \frac{1}{J_e} \sum_{j=1}^{3} \tilde{\partial}_j (\widetilde{L}_j \widetilde{\nabla} \mathbf{w}), \quad \widetilde{L}_j \widetilde{\nabla} \mathbf{w} = \sum_{k=1}^{3} N^{jk} \tilde{\partial}_k \mathbf{w}. \tag{40}$$

The 3×3 matrices N^{jk} are related to M^{qp} according to

$$N^{jk} = J_e \sum_{q=1}^{3} \sum_{p=1}^{3} \beta_q^j \beta_p^k M^{qp}.$$

One can show that the matrices N^{jk} have the same properties as M^{jk}, i.e., N^{kk} are symmetric and positive definite, and $N^{kj} = (N^{jk})^T$, see [27] for details.

An energy estimate can be derived in the same way as in the Cartesian case, because the factor J_e in the scalar product cancels the factor $1/J_e$ the curvilinear spatial operator (40). Partial integration gives the interior term

$$S_p(\mathbf{w}_t,\mathbf{w}) = \iiint_{r_3=0}^{\infty} \begin{pmatrix} \tilde{\partial}_1\mathbf{w}_t^T & \tilde{\partial}_2\mathbf{w}_t^T & \tilde{\partial}_3\mathbf{w}_t^T \end{pmatrix} \begin{pmatrix} N^{11} & N^{12} & N^{13} \\ N^{21} & N^{22} & N^{23} \\ N^{31} & N^{32} & N^{33} \end{pmatrix} \begin{pmatrix} \tilde{\partial}_1\mathbf{w} \\ \tilde{\partial}_2\mathbf{w} \\ \tilde{\partial}_3\mathbf{w} \end{pmatrix} dr_1\, dr_2\, dr_3,$$

which is of the form (23). The main difference is that the matrices M^{jk}, which describe the material properties in the Cartesian case, are replaced by the matrices N^{jk}, which describe the corresponding material properties in parameter space. By extracting the factor J_e that is included in N^{jk} and noting that the volume element satisfies $d\Omega = J_e dr_1 dr_2 dr_3$, we see that $S_p(\mathbf{w}_t,\mathbf{w}) = S(\mathbf{w}_t,\mathbf{w})$. In particular, the interior term $S_p(\mathbf{v},\mathbf{w})$ is symmetric in its arguments and positive semi-definite.

The energy balance equation corresponding to (24) has a boundary term of the form

$$-\iint \mathbf{w}_t \cdot \widetilde{L}_3\widetilde{\nabla}\mathbf{w}\Big|_{r_3=0} dr_1 dr_2. \tag{41}$$

The outwards normal along $r_3 = 0$ satisfies $\mathbf{n}_e = -\mathbf{b}^3/|\mathbf{b}^3|$. By using the technique in reference [27], one can show

$$\mathscr{T}\cdot\mathbf{n}_e = -\frac{1}{|\mathbf{b}^3|J_e}\widetilde{L}_3\widetilde{\nabla}\mathbf{w}, \quad r_3 = 0. \tag{42}$$

Similar to the boundary term in the acoustic domain, the surface element satisfies $d\Gamma = |\mathbf{b}^3|J_e\, dr_1 dr_2$. We conclude that (41) equals the boundary term on the right hand side of (24).

4.3 The interface conditions in curvilinear coordinates

By using $\tilde{C} = |\mathbf{a}^3|J\widehat{A}$ and $\hat{\rho}\mathbf{q}\cdot\widehat{A}\mathbf{q} = 2p(\mathbf{u}\cdot\mathbf{n}_a)$, the sum of the boundary terms (38) and (41) can be written

$$BT := -\iint \Big[p(\mathbf{u}\cdot\mathbf{n}_a)|\mathbf{a}^3|J + \mathbf{w}_t\cdot\widetilde{L}_3\widetilde{\nabla}\mathbf{w}\Big]_{r_3=0} dr_1\, dr_2.$$

If we assume continuity of normal velocity, i.e., $\mathbf{w}_t\cdot\mathbf{n}_e = -\mathbf{u}\cdot\mathbf{n}_a$, the integrand in BT becomes

$$\mathbf{w}_t\cdot\Big[-p|\mathbf{a}^3|J\mathbf{n}_e + \widetilde{L}_3\widetilde{\nabla}\mathbf{w}\Big].$$

Thus, $BT = 0$ if we enforce the curvilinear interface conditions

$$\begin{cases} \widetilde{L}_3\widetilde{\nabla}\mathbf{w} = -p|\mathbf{a}^3|J\mathbf{n}_a, \\ \mathbf{w}_t\cdot\mathbf{n}_e = -\mathbf{u}\cdot\mathbf{n}_a, \end{cases} \qquad r_3 = 0,\ \ t > 0. \tag{43}$$

By using (42) and $\mathbf{n}_a = -\mathbf{n}_e$, we see that the first condition can be written

$$-|\mathbf{b}^3|J_e(\mathscr{T}\cdot\mathbf{n}_e) = p|\mathbf{a}^3|J\mathbf{n}_e.$$

The first two covariant base vectors only depend on tangential derivatives along the interface, and must therefore be equal in the atmospheric and solid earth sub-domains, on either side of the interface. Because of the metric identity (30), we therefore conclude that $|\mathbf{a}^3|J = |\mathbf{b}^3|J_e$. Thus the curvilinear interface conditions (43) are equivalent to (10).

When the interface conditions (43) are satisfied, we arrive at an energy balance equation in curvilinear coordinates that is completely analogous to (27),

$$\frac{1}{2}\frac{d}{dt}\Big((\rho_e\mathbf{w}_t,\mathbf{w}_t)_{P_e} + S_p(\mathbf{w},\mathbf{w}) + (\hat{\rho}\mathbf{q},\mathbf{q})_{P_a}\Big) = -(\hat{\rho}\mathbf{q},H\mathbf{q})_{P_a} + (\hat{\rho}\mathbf{q},\mathbf{f})_{P_a} + (\mathbf{w}_t,\mathbf{g})_{P_e}. \tag{44}$$

5 Discretization in space

Before presenting the spatial discretization of the 3-D seismo-acoustic system in curvilinear coordinates, we first review some properties of summation-by-parts (SBP) finite difference operators in one space dimension.

5.1 SBP finite difference operators in 1D

Assume that a one dimensional domain is discretized on a uniform grid $x_i = ih$ for $i = 0,\dots,n$, where the domain boundaries are at $i = 0$ and $i = n$. Let u_i be a real-valued function defined on the grid. We say that the difference operator D, approximating d/dx, satisfies the SBP property if,

$$(u,Dv)_{h1} = -(Du,v)_{h1} - u_0v_0 + u_nv_n, \tag{45}$$

in a weighted discrete scalar product,

$$(u,v)_{h1} = h\sum_{i=0}^{n} \omega_i u_i v_i, \quad 0 < \omega_i < \infty, \tag{46}$$

where ω_i are the weights. The grid function Du_i is defined at all points $i = 0\dots,n$. Away from the boundaries, Du_i equals a centered difference operator and $\omega_i = 1$. For example, the fourth and sixth order accurate stencils are

$$D^{\{4\}}q_j = D_0\left(I - \frac{h^2}{6}D_+D_-\right)q_j, \quad j\in[4,n-4], \tag{47}$$

$$D^{\{6\}}q_j = D_0\left(I - \frac{h^2}{6}D_+D_- + \frac{h^4}{30}D_+^2D_-^2\right)q_j, \quad j\in[6,n-6], \tag{48}$$

where the forwards, backwards, and centered difference operators are $D_+q_j = (q_{j+1}-q_j)/h$, $D_-q_j = D_+q_{j-1}$, and $D_0q_j = 0.5(q_{j+1}-q_{j-1})/h$, respectively. The stencils near the boundaries can be found in Strand [31].

In order to satisfy (45), the coefficients in D are modified at a few points near each boundary. When using a scalar product of the form (46), it is well known that (45) can only be satisfied if the order of the truncation error in Du is reduced by a factor of two at a few points near each boundary. It is possible to improve the truncation error near the boundary by using so-called full norm SBP operators [31]. However, these operators can lead to instabilities with variable coefficients and will not be used here. In the following our presentation assumes a scalar product of the form (46).

SBP operators of accuracy order $\mathscr{O}(h^p)$ away from the boundaries and order $\mathscr{O}(h^{p/2})$ near the boundaries are well-known for $p = 2,4,6,8$, see e.g. [31]. It is theoretically possible to derive even higher order accurate SBP operators, but the stencils become very wide and the coefficients depend on a number of parameters that can be difficult to determine.

Second derivative terms of the type $(a(x)u_x)_x)$ appear in the elastic wave equation. Here $a(x)$ is a known function that describes a material property such as the shear modulus. These terms could be approximated by applying D twice. However, this approach leads to difficulties with odd-even modes, meaning that the null space of $D(aDu)_j$ contains highly oscillatory grid functions. Furthermore, because of the boundary modification, the truncation error of D is not smooth near the boundary, leading to additional loss of accuracy during its second application.

In [28], we constructed a difference operator $G(a)u$ approximating $(a(x)u_x)_x$, which does not have problems with odd-even modes. This operator satisfies the SBP identity

$$(v,G(a)u)_{h1} = -(Dv,aDu)_{h1} + (v,P(a)u)_{hr1} - v_0a_0S^bu_0 + v_na_nS^bu_n. \tag{49}$$

Here, the positive semi-definite operator $P(a)$ is small for smooth grid functions and non-zero for odd-even modes , see [28] for details. The boundary operator

$$S^bu_0 = \frac{1}{h}\sum_{k=-1}^{m} \sigma_k u_k, \tag{50}$$

is an approximation of $u_x(x_0)$ and $S^b u_n$ is the corresponding approximation of $u_x(x_n)$. The boundary operators have full order of accuracy, $\mathcal{O}(h^p)$. Note that $S^b u_0$ makes use of the ghost point value u_{-1}, because $\sigma_{-1} \neq 0$. The operator $S^b u_n$ is similar, and uses the ghost point value u_{n+1}. For 4th order accuracy, the coefficients are

$$\sigma_{-1} = -\frac{1}{4},\ \ \sigma_0 = -\frac{5}{6},\ \ \sigma_1 = \frac{3}{2},\ \ \sigma_2 = -\frac{1}{2},\ \ \sigma_3 = \frac{1}{12}.$$

The operator $G(a)$, derived in [28], is fourth order accurate in the interior and second order near the boundary. In the interior of the domain, it reverts to the centered five point formulae

$$G(a)w_j = \frac{1}{6h^2}\left[c_{-2}(w_{j-2} - w_j) + c_{-1}(w_{j-1} - w_j) + c_1(w_{j+1} - w_j) + c_2(w_{j+2} - w_j)\right],$$

for $j \in [6, n-6]$, where

$$\begin{aligned} c_{-2} &= a_{j-1} - 0.75(a_j + a_{j-2}),\ \ c_{-1} = a_{j-2} + a_{j+1} + 3(a_j + a_{j-1}),\\ c_1 &= a_{j+2} + a_{j-1} + 3(a_{j+1} + a_j),\ \ c_2 = a_{j+1} - 0.75(a_j + a_{j+2}). \end{aligned}$$

Near the boundary, the difference formula can be written as

$$G(a)w_j = \frac{1}{h^2}\sum_{k=0}^{7}\sum_{m=0}^{7} b_{j,k,m} a_m w_k, \quad j = 0, \ldots, 5.$$

In this expression, 129 out of the 384 entries in $b_{j,k,m}$ are non-zero, see [28] for details.

Because the elastic wave equation is solved in second order formulation, the solution becomes up to two orders of accuracy more accurate than the truncation error near the boundary [32]. For example, the difference operator $G(a)$ has a fourth order truncation error in the interior of the domain and a second order truncation error near the boundary. In this case, the solution becomes fourth order accurate in maximum norm [28]. The approach can be extended to even higher orders of accuracy. For example, SBP operators for second derivatives have been derived with up to eighth higher order of accuracy [15]; sixth order accurate SBP operators have been used to solve the elastic wave equation [8].

5.2 The linearized Euler equations

In the atmospheric domain we discretize the parameter space on a grid with constant grid size $h > 0$. When possible, we use multi-index notation to condense the notation. The grid points have parameter coordinates

$$\mathbf{r}_\mathbf{i} = (r_{1,i}, r_{2,j}, r_{3,k})^T, \quad \mathbf{i} = (i, j, k), \quad r_{1,i} = ih, \quad r_{2,j} = jh, \quad r_{3,k} = kh. \tag{51}$$

We define two partially overlapping sets of grid points,

$$I_{\Omega_a} = \{(i, j) = 0, \pm 1, \pm 2, \ldots,\ \ k = 0, -1, -2, \ldots\}, \tag{52}$$

$$I_\Gamma = \{(i, j) = 0, \pm 1, \pm 2, \ldots,\ \ k = 0\}. \tag{53}$$

The physical coordinates of the grid points follow from the mapping, $\mathbf{x}_\mathbf{i} = \mathbf{x}(\mathbf{r}_\mathbf{i})$. We denote a grid function by $\mathbf{u}_\mathbf{i} = \mathbf{u}_{i,j,k} = \mathbf{u}(\mathbf{x}_\mathbf{i})$, and approximate $\tilde{\partial}_j \mathbf{u}$ by the difference operator $D_j \mathbf{u}$, which is defined component-wise.

The semi-discrete approximation of the linearized Euler equations in density scaled split form and curvilinear coordinates becomes,

$$\frac{d\mathbf{q}_\mathbf{i}}{dt} = \mathbf{K}_h \mathbf{q}_\mathbf{i} + \mathbf{f}_\mathbf{i}, \quad \mathbf{i} \in I_{\Omega_a},\ \ t > 0, \tag{54}$$

where

$$\mathbf{K}_h \mathbf{q} = -\frac{1}{2J}\left[\tilde{A} D_1 \mathbf{q} + \tilde{B} D_2 \mathbf{q} + \tilde{C} D_3 \mathbf{q}\right] - \frac{1}{2\hat{\rho} J}\left[D_1\left(\hat{\rho}\tilde{A}\mathbf{q}\right) + D_2\left(\hat{\rho}\tilde{B}\mathbf{q}\right) + D_3\left(\hat{\rho}\tilde{C}\mathbf{q}\right)\right] - H\mathbf{q}. \tag{55}$$

For the upper half-space domain we define a discrete scalar product for real-valued grid functions **u** and **v** by

$$(\mathbf{u},\mathbf{v})_U = h^3 \sum_{i,j} \sum_{k=-\infty}^{0} \gamma_k \mathbf{u}_{i,j,k} \cdot \mathbf{v}_{i,j,k}. \tag{56}$$

Here $\gamma_k > 0$ are the weights corresponding to ω_k in (46). The only boundary corresponds to $k = 0$, so the vector version of the SBP identity (45) becomes

$$(\mathbf{u}, D_1\mathbf{v})_U = -(D_1\mathbf{u},\mathbf{v})_U, \tag{57}$$

$$(\mathbf{u}, D_2\mathbf{v})_U = -(D_2\mathbf{u},\mathbf{v})_U, \tag{58}$$

$$(\mathbf{u}, D_3\mathbf{v})_U = -(D_3\mathbf{u},\mathbf{v})_U + h^2 \sum_{i,j} \mathbf{u}_{i,j,0} \cdot \mathbf{v}_{i,j,0}, \tag{59}$$

as can be seen by component-wise application of the corresponding scalar identities.

Corresponding to the continuous scalar product in curvilinear coordinates (37), we derive an energy estimate for the semi-discrete problem in the scaled discrete scalar product

$$(\mathbf{u},\mathbf{v})_{H_a} := (\mathbf{u}, J\mathbf{v})_U = h^3 \sum_{i,j} \sum_{k=-\infty}^{0} \gamma_k J_{i,j,k} \mathbf{u}_{i,j,k} \cdot \mathbf{v}_{i,j,k}. \tag{60}$$

Let the grid function $\mathbf{q}_{\mathbf{i}}(t)$ be a solution of (54) and consider

$$\frac{1}{2}\frac{d}{dt}(\hat{\rho}\mathbf{q},\mathbf{q})_{H_a} = \left(\hat{\rho}\mathbf{q}, \frac{d\mathbf{q}}{dt}\right)_{H_a}.$$

We start by substituting $d\mathbf{q}/dt$ by the right hand side of (54). As in the continuous case, the factor J in the scalar product cancels the factor $1/J$ in the first two terms of (55). We then apply the SBP relations (57)-(59) on the second term. The only boundary contribution arises from the terms containing D_3,

$$T_{\mathbf{i}} := -\frac{1}{2J_{\mathbf{i}}}\tilde{C}_{\mathbf{i}} D_3 \mathbf{q}_{\mathbf{i}} - \frac{1}{2\hat{\rho}_{\mathbf{i}} J_{\mathbf{i}}} D_3 \left(\hat{\rho}\tilde{C}\mathbf{q}\right)_{\mathbf{i}}.$$

By using (59) and that the matrix $\tilde{C}$ is symmetric,

$$(\hat{\rho}\mathbf{q}, T)_{H_a} = -\frac{1}{2}\left(\hat{\rho}\mathbf{q}, \tilde{C} D_3 \mathbf{q}\right)_U - \frac{1}{2}\left(\mathbf{q}, D_3\left(\hat{\rho}\tilde{C}\mathbf{q}\right)\right)_U = -\frac{h^2}{2}\sum_{i,j}\left(\hat{\rho}\mathbf{q}\cdot\tilde{C}\mathbf{q}\right)_{i,j,0}.$$

Thus, the energy balance for the semi-discrete problem (54) becomes

$$\frac{1}{2}\frac{d}{dt}(\hat{\rho}\mathbf{q},\mathbf{q})_{H_a} = -\frac{h^2}{2}\sum_{i,j}\left(\hat{\rho}\mathbf{q}\cdot\tilde{C}\mathbf{q}\right)_{i,j,0} - (\hat{\rho}\mathbf{q}, H\mathbf{q})_{H_a} + (\hat{\rho}\mathbf{q},\mathbf{f})_{H_a}. \tag{61}$$

5.3 The elastic wave equation

The parameter space in the solid earth sub-domain is discretized on a grid with the same grid size ($h > 0$) as in the atmospheric domain,

$$r_{1,i} = ih, \quad r_{2,j} = jh, \quad r_{3,k} = kh. \tag{62}$$

We group the grid points into the disjoint sets of interior and ghost points,

$$I_{\Omega_e} = \{(i,j) = 0, \pm 1, \pm 2, \ldots, \ k = 0,1,2,\ldots\}, \tag{63}$$

$$I_{\Gamma,ghost} = \{(i,j) = 0, \pm 1, \pm 2, \ldots, \ k = -1\}. \tag{64}$$

The grid point coordinates in the physical domain following by applying the mapping function, $\mathbf{x}_{e,\mathbf{i}} = \mathbf{x}_e(\mathbf{r}_{\mathbf{i}})$.

We write the spatial discretization of the elastic wave equation in curvilinear coordinates as

$$\rho_{e,\mathbf{i}}\frac{d^2\mathbf{w}_\mathbf{i}}{dt^2} = \mathbf{L}_h\mathbf{w}_\mathbf{i} + \mathbf{g}_\mathbf{i}, \quad \mathbf{i} \in I_{\Omega_e},\ t > 0, \tag{65}$$

where the discrete spatial operator is

$$\begin{aligned}\mathbf{L}_h\mathbf{w} = \frac{1}{J_{e,\mathbf{i}}}\big[&G_1(N^{11})\mathbf{w} + G_2(N^{22})\mathbf{w} + G_3(N^{33})\mathbf{w}\\ &+ D_1(N^{12}D_2\mathbf{w}) + D_1(N^{13}D_3\mathbf{w}) + D_2(N^{21}D_1\mathbf{w}) + D_2(N^{23}D_3\mathbf{w})\\ &+ D_3(N^{31}D_1\mathbf{w}) + D_3(N^{32}D_2\mathbf{w})\big].\end{aligned} \tag{66}$$

Similar to the linearized Euler equations, $D_m\mathbf{w}$ approximates $\tilde{\partial}_m\mathbf{w}$ (but possibly to a different order of accuracy). This operator is used to approximate the terms $\tilde{\partial}_i(N^{ij}\tilde{\partial}_j\mathbf{w})$ when $i \neq j$. However, when $i = j$, the term is approximated by $G_i(N^{ii})\mathbf{w}$, with components

$$G_i(N^{ii})\mathbf{w} := \begin{pmatrix}(G_i(N^{ii})\mathbf{w})_1\\(G_i(N^{ii})\mathbf{w})_2\\(G_i(N^{ii})\mathbf{w})_3\end{pmatrix}, \quad (G_i(N^{ii})\mathbf{w})_p = \sum_{q=1}^{3} G_i(\eta^{ii}_{pq})w^{(q)}, \quad p = 1,2,3. \tag{67}$$

Here, η^{ii}_{pq} are the elements of the 3×3 matrix N^{ii} and $G_i(\eta^{ii}_{pq})w^{(q)}$ is the scalar difference operator described in § 5.1, applied in direction i. The components of the displacement vector are $\mathbf{w} = (w^{(1)}, w^{(2)}, w^{(3)})^T$.

We define the discrete scalar product for real-valued grid functions in the lower half-space by

$$(\mathbf{u},\mathbf{v})_L = h^3\sum_{i,j}\sum_{k=0}^{\infty}\omega_k\mathbf{u}_{i,j,k}\cdot\mathbf{v}_{i,j,k}. \tag{68}$$

Note that the weights ω_k are different from γ_k in (56) when different orders of accuracy are used in the two subdomains. Again, the only boundary corresponds to $k = 0$, but the boundary term changes sign from (59),

$$(\mathbf{u}, D_3\mathbf{v})_L = -(D_3\mathbf{u},\mathbf{v})_L - h^2\sum_{i,j}\mathbf{u}_{i,j,0}\cdot\mathbf{v}_{i,j,0}, \tag{69}$$

The vector version of the SBP identity (49) becomes

$$(\mathbf{v}, G_1(N)\mathbf{w})_L = -(D_1\mathbf{v}, ND_1\mathbf{w})_L + (\mathbf{v}, P_1(N)\mathbf{w})_{L_r}, \tag{70}$$

$$(\mathbf{v}, G_2(N)\mathbf{w})_L = -(D_2\mathbf{v}, ND_2\mathbf{w})_L + (\mathbf{v}, P_2(N)\mathbf{w})_{L_r}, \tag{71}$$

$$(\mathbf{v}, G_3(N)\mathbf{w})_L = -(D_3\mathbf{v}, ND_3\mathbf{w})_L + (\mathbf{v}, P_3(N)\mathbf{w})_{L_r} - h^2\sum_{i,j}\Big(\mathbf{v}_{i,j,0}\cdot NS^b\mathbf{w}\Big)_{i,j,0}, \tag{72}$$

as can be seen by component-wise application of the corresponding scalar identities. Here $(\cdot,\cdot)_{L_r}$ is the 3-D scalar product corresponding to $(\cdot,\cdot)_{hr}$.

We derive an energy estimate for the semi-discrete elastic wave equation in curvilinear coordinates using the Jacobian-weighted discrete scalar product

$$(\mathbf{u},\mathbf{v})_{H_e} := (\mathbf{u}, J_e\mathbf{v})_L = h^3\sum_{i,j}\sum_{k=0}^{\infty}\omega_k J_{e,i,j,k}(\mathbf{u}_{i,j,k}\cdot\mathbf{v}_{i,j,k}). \tag{73}$$

Let the grid function $\mathbf{w}_\mathbf{i}(t)$ be a solution of (65)-(66) and consider

$$\frac{1}{2}\frac{d}{dt}(\rho_e\mathbf{w}_t, \mathbf{w}_t)_{H_e} = (\mathbf{w}_t, \mathbf{L}_h\mathbf{w})_{H_e} + (\mathbf{w}_t, \mathbf{g})_{H_e}.$$

In [27] we show that the SBP properties (69)-(72) give the decomposition

$$(\mathbf{w}_t, \mathbf{L}_h\mathbf{w})_{H_e} = -S_h(\mathbf{w}_t, \mathbf{w}) + B_h(\mathbf{w}_t, \mathbf{w}).$$

Similar to the continuous case, S_h holds interior terms that represent the elastic potential energy, and B_h contains boundary terms. As before, S_h is symmetric in its arguments and positive semi-definite. Because the elastic sub-domain only has one boundary, the expression from [27] simplifies to

$$B_h(\mathbf{w}_t,\mathbf{w}) = -h^2 \sum_{i,j} \left(\mathbf{w}_t \cdot \widetilde{L}_{3,h} \widetilde{\nabla}_h \mathbf{w} \right)_{i,j,0}, \tag{74}$$

$$\widetilde{L}_{3,h} \widetilde{\nabla}_h \mathbf{w} = N^{31} D_1 \mathbf{w} + N^{32} D_2 \mathbf{w} + N^{33} S_3^b \mathbf{w}. \tag{75}$$

Here, $S_3^b \mathbf{w}$ is the boundary operator (50) applied to each component of $\mathbf{w}$ to approximate $\tilde{\partial}_3 \mathbf{w}$.

5.4 The discrete interface conditions

By comparing (75) and (42), we see that the former is an approximation of the boundary traction, scaled by $J_e|\mathbf{b}^3|$. To make this obvious, we can write the sum on the right hand side of (74) as

$$-h^2 \sum_{i,j} \left(J_e |\mathbf{b}^3| \mathbf{w}_t \cdot \frac{1}{J_e|\mathbf{b}^3|} \widetilde{L}_{3,h} \widetilde{\nabla}_h \mathbf{w} \right)_{i,j,0} = h^2 \sum_{i,j} \left(J_e |\mathbf{b}^3| \mathbf{w}_t \cdot (\mathscr{T}_h \cdot \mathbf{n}_e) \right)_{i,j,0}, \tag{76}$$

where

$$\mathscr{T}_h \cdot \mathbf{n}_e := -\frac{1}{J_e|\mathbf{b}^3|} \widetilde{L}_{3,h} \widetilde{\nabla}_h \mathbf{w}, \tag{77}$$

is the discretization of the boundary traction (42).

By using the same technique as in § 4.3, we conclude that the discretized coupled seismo-acoustic system satisfies the energy balance equation,

$$\frac{1}{2}\frac{d}{dt}\Big((\rho_e \mathbf{w}_t, \mathbf{w}_t)_{H_e} + S_h(\mathbf{w},\mathbf{w}) + (\hat{\rho}\mathbf{q},\mathbf{q})_{H_a} \Big) = -(\hat{\rho}\mathbf{q}, H\mathbf{q})_{H_a} + (\hat{\rho}\mathbf{q},\mathbf{f})_{H_a} + (\mathbf{w}_t,\mathbf{g})_{H_e}, \tag{78}$$

when the discrete interface conditions

$$\begin{cases} \widetilde{L}_{3,h} \widetilde{\nabla}_h \mathbf{w}\Big|_{\mathbf{i}} = -p|\mathbf{a}^3| J \mathbf{n}_a\Big|_{\mathbf{i}}, \\ \mathbf{w}_t \cdot \mathbf{n}_e\big|_{\mathbf{i}} = -\,\mathbf{u}\cdot\mathbf{n}_a\big|_{\mathbf{i}}, \end{cases} \qquad \mathbf{i} \in I_\Gamma, \;\; t > 0. \tag{79}$$

are satisfied. Since the rate of total discrete energy (78) only depends on a zeroth order term, Gronwall's lemma [12] can be used to show that the spatial discretization of the coupled seismo-acoustic problem is stable.

6 Time integration

In order to use the same time integration method on both sub-domains, we rewrite the discretized elastic wave equation as a system with first derivatives in time. By introducing the auxiliary variable $\mathbf{v} = \mathbf{w}_t$ into (65), we get

$$\begin{cases} \rho_{e,\mathbf{i}} \dfrac{d\mathbf{v}_{\mathbf{i}}}{dt} = \mathbf{L}_h \mathbf{w}_{\mathbf{i}} + \mathbf{g}_{\mathbf{i}}, \\ \dfrac{d\mathbf{w}_{\mathbf{i}}}{dt} = \mathbf{v}_{\mathbf{i}}, \end{cases} \qquad \mathbf{i} \in I_{\Omega_e}, \;\; t > 0. \tag{80}$$

In terms of the auxiliary variable, the interface condition (79) becomes

$$\widetilde{L}_{3,h} \widetilde{\nabla}_h \mathbf{w}\Big|_{\mathbf{i}} = -p|\mathbf{a}^3| J \mathbf{n}_a\Big|_{\mathbf{i}}, \tag{81}$$

$$\mathbf{v}_{\mathbf{i}} \cdot \mathbf{n}_a = \mathbf{u}_{\mathbf{i}} \cdot \mathbf{n}_a, \tag{82}$$

for $\mathbf{i} \in I_\Gamma$ (using $\mathbf{n}_e = -\mathbf{n}_a$).

We use the classical explicit 4th order Runge-Kutta (RK-4) method to simultaneously time-integrate (80) and the discretized linearized Euler equation (54). For simplicity, the same time step is used in both domains.

6.1 Enforcing the interface conditions

A coupled fluid-structure problem can become stiff unless the interface conditions are enforced in the correct sequence. The stiffness is avoided when the normal stress on the interface is determined by the lighter material and the normal velocity of the interface is determined by the heavier material [5]. At an acoustic/elastic interface it typically holds that $\hat{\rho} \ll \rho_e$. Hence, we let the atmospheric pressure determine the elastic normal stresses, and the elastic normal velocity determine the normal velocity in the atmosphere.

Each stage of the RK-4 time-stepping consists of advancing the solution at all interior grid points, followed by enforcing the interface conditions. These are the same steps as in the Euler forward method, which is more straightforward to describe in detail. Note, however, that the Euler forward method is unstable for hyperbolic wave propagation problems, due to the purely imaginary eigenvalues of the spatial operator.

We discretize time on a uniform grid, $t_n = n\Delta_t$, with a constant time step $\Delta_t > 0$, and denote a time-discrete grid function by $\mathbf{q}_{\mathbf{i}}^n \approx \mathbf{q}_{\mathbf{i}}(t_n)$. The Euler forward method for solving (54) and (80), coupled by the discrete interface conditions (81)-(82), consists of two steps. Given $(\mathbf{q}_{\mathbf{i}}^n, \mathbf{v}_{\mathbf{i}}^n, \mathbf{w}_{\mathbf{i}}^n)$, we first update the solution at the interior grid points in both domains,

$$\mathbf{q}_{\mathbf{i}}^* = \mathbf{q}_{\mathbf{i}}^n + \Delta_t \left(\mathbf{K}_h \mathbf{q}_{\mathbf{i}}^n + \mathbf{f}_{\mathbf{i}}^n \right), \qquad \mathbf{i} \in I_{\Omega_a}, \tag{83}$$

$$\mathbf{v}_{\mathbf{i}}^{n+1} = \mathbf{v}_{\mathbf{i}}^n + \frac{\Delta_t}{\rho_{e,\mathbf{i}}} \left(\mathbf{L}_h \mathbf{w}_{\mathbf{i}}^n + \mathbf{g}_{\mathbf{i}}^n \right), \quad \mathbf{i} \in I_{\Omega_e}, \tag{84}$$

$$\mathbf{w}_{\mathbf{i}}^{n+1} = \mathbf{w}_{\mathbf{i}}^n + \Delta_t \mathbf{v}_{\mathbf{i}}^n, \qquad \mathbf{i} \in I_{\Omega_e}. \tag{85}$$

Note that (83) can be evaluated at all interior grid points given $\mathbf{q}_{\mathbf{i}}^n$, $\mathbf{i} \in I_{\Omega_a}$. However, in order to evaluate (84) on the interface, we must provide both interior and ghost point values for $\mathbf{w}_{\mathbf{i}}^n$, i.e., $\mathbf{i} \in I_{\Omega_e} \cup I_{\Gamma,ghost}$.

The interface condition (81) is enforced as follows. We have $\mathbf{q}^* = (s^*, \mathbf{u}^*, r^*)^T$, where s^* and r^* can be used to calculate p^* from (11). Given p^* on the interface, the ghost point values of $\mathbf{w}^{n+1}$ are determined to satisfy

$$\widetilde{L}_{3,h} \widetilde{\nabla}_h \mathbf{w}_{\mathbf{i}}^{n+1} = -p_{\mathbf{i}}^* (|\mathbf{a}^3| J \mathbf{n}_a)_{\mathbf{i}}, \quad \mathbf{i} \in I_\Gamma.$$

Because the term $\widetilde{L}_{3,h} \widetilde{\nabla}_h \mathbf{w}_{\mathbf{i}}$ involves the boundary difference term $S_3^b \mathbf{w}_{\mathbf{i}}$, this condition corresponds to three linear equations for the three components of the unknown vector $\mathbf{w}_{i,j,-1}^{n+1}$, at each grid point along the interface. There is no coupling of the unknowns along the interface.

We use the projection method [19], [20] to enforce the second interface condition (82). To decompose the velocity into its normal and tangential components, we define the 3×3 projection matrix $P = \mathbf{n}_a \mathbf{n}_a^T$. It uniquely defines the decomposition of a 3-vector $\mathbf{u} = \mathbf{u}^I + \mathbf{u}^{II}$, by $\mathbf{u}^I = P\mathbf{u}$, and $\mathbf{u}^{II} = (I - P)\mathbf{u}$. Hence, $\mathbf{u}^I = (\mathbf{u} \cdot \mathbf{n}_a)\mathbf{n}_a$ is the normal component of $\mathbf{u}$ and $\mathbf{u}^{II} = \mathbf{u} - \mathbf{u}^I$ is its tangential component. The interface condition is then enforced by

$$\mathbf{u}_{\mathbf{i}}^{n+1} = \begin{cases} (I - P)\mathbf{u}_{\mathbf{i}}^* + P\mathbf{v}_{\mathbf{i}}^{n+1}, & \mathbf{i} \in I_\Gamma, \\ \mathbf{u}_{\mathbf{i}}^*, & \mathbf{i} \in (I_{\Omega_a} \cap I_\gamma), \end{cases}$$

The remaining components of $\mathbf{q}^{n+1}$ are defined by

$$s_{\mathbf{i}}^{n+1} = s_{\mathbf{i}}^*, \quad r_{\mathbf{i}}^{n+1} = r_{\mathbf{i}}^*, \quad \mathbf{i} \in I_{\Omega,a}.$$

This completes one time step of the Euler forward method. In the RK-4 method, the interface conditions are enforced after each of the four stages.

6.2 Estimating the time step

As with all explicit time stepping methods, the time step must not exceed the CFL stability limit. In the acoustic sub-domain, the stability limit can be determined from the eigenvalues of the spatial operator $\mathbf{K}_h$ in (54). When the background flow field varies in space, the eigenvalues are estimated by a von Neumann analysis, i.e., by locally freezing the coefficients and Fourier transforming the difference operators. For a Cartesian mesh, this leads to

$$\kappa_a = \max_{i,j,k} \left(|\hat{u}_1 + \hat{c}| + |\hat{u}_2 + \hat{c}| + |\hat{u}_3 + \hat{c}| \right),$$

where the maximum is taken over all grid points in the acoustic sub-domain. This leads to the acoustic stability restriction for the time-step,

$$\Delta_{t,a} \leq C_{fl} \frac{h}{\kappa_a},$$

where $C_{fl} > 0$ is the CFL number. For the elastic sub-domain, we apply a similar approach to estimate the largest eigenvalue of the spatial operator $\mathbf{L}_h/\rho_e$. For a Cartesian mesh, this gives

$$\kappa_e = \frac{16}{3} \max_{i,j,k} \frac{\lambda + 4\mu}{\rho_e}.$$

Here, the maximum is evaluated over all grid points in the elastic sub-domain. The resulting time-step stability restriction becomes

$$\Delta_{t,e} \leq C_{fl} \frac{h}{\sqrt{\kappa_e}}.$$

The time step for the coupled seismo-acoustic time-stepping is finally taken to be

$$\Delta_t = \min\left(\Delta_{t,a},\, \Delta_{t,e}\right), \quad C_{fl} = 1.1. \tag{86}$$

The CFL-number was determined by numerical experiments. It is straightforward to generalize the above approach to estimate the time step for a curvilinear mesh.

7 Numerical experiments

The numerical experiments in this section were performed with version 1.0 of the elastic-acoustic simulation code ElAc [30]. This code has been verified extensively, but to conserve space we only present a few of the tests here. We also demonstrate the capabilities of the proposed numerical method by presenting a coupled wave propagation simulation due to a bursting bolide.

7.1 The computational domain and far-field treatment

Before any computer simulations can be performed, the computational domain must be truncated to a finite extent and this can be done in many different ways. Here we use the super-grid technique [2], [25], [27], which combines grid stretching and artificial dissipation to slow down and damp out waves that leave the computational domain. Homogeneous Dirichlet boundary conditions are imposed at a sufficient number of ghost points outside the super-grid layers, avoiding the use of boundary-modified SBP difference operators at the outer boundaries. This technique significantly simplifies the implementation of the method and is provable stable [25]. The stability of the super-grid technique holds both for the linearized Euler equations and the elastic wave equation in general anisotropic materials. It has been numerically demonstrated that artificial reflections can be made to converge to zero at the same rate as the truncation error of the interior scheme [25], [27]. For the purpose of practical seismic wave simulations with a fourth order method, it is usually adequate to have 30 grid points in the super-grid layers.

Figure 2 outlines the computational domain for the coupled seismo-acoustic problem. We consider box-shaped domains that cover (in Cartesian coordinates) $0 \leq x_1 \leq x_{max}$, $0 \leq x_2 \leq y_{max}$, and $z_{min} \leq x_3 \leq z_{max}$. When the interface is planar, we assume it is located along $x_3 = 0$, such that the atmospheric domain occupies $z_{min} \leq x_3 \leq 0$ and the solid earth is in $0 \leq x_3 \leq z_{max}$. In this case the maximum altitude in the atmospheric domain is $-z_{min}$, and the solid earth extends to the depth z_{max}. When the interface is non-planar, we discretize the elastic and atmospheric sub-domains with curvilinear grids that conform to the interface. In parameter space the topographic interface is always flat.

The elastic wave equation is discretized by SBP finite difference operators that are fourth order accurate in the interior of the domain, with second order accurate boundary modifications. When used to only solve the elastic wave equation, this discretization gives overall fourth order convergence rate in max-norm, see [28]. In the atmospheric domain, the discretization uses a sixth order accurate SBP finite difference operator in the interior of the domain, with third order accuracy near the boundaries. Standard convergence results for first order hyperbolic problems indicate that the actual convergence rate should be one order higher than the boundary accuracy [11]. As

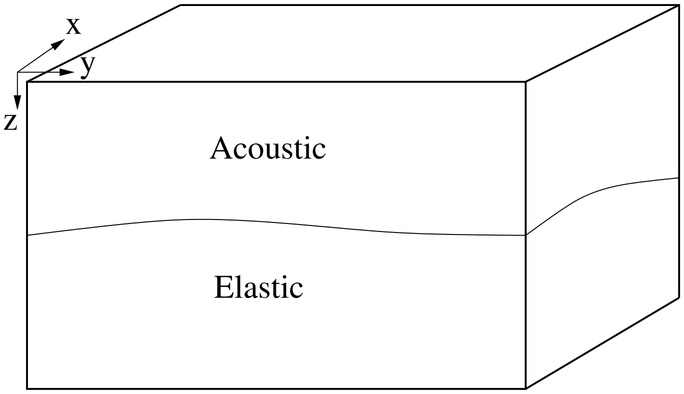

Figure 2: The topographic interface $x_3 = \tau(x_1, x_2)$ separates the atmospheric domain (Ω_a) and the elastic domain (Ω_e).

a result, overall fourth order accuracy should be expected also in the atmospheric domain. However, the numerical examples shown below indicate that the accuracy assertion is only partly true.

The atmospheric and elastic domains are discretized by grids that are uniform in parameter space, both with grid spacing h. In the atmospheric domain, the grid has $N_1^A \times N_2^A \times N_3^A$ points, and in the elastic domain the number of grid points are $N_1^E \times N_2^E \times N_3^E$. The number of grid points are the same in the horizontal directions, i.e., $N_1^A = N_1^E$ and $N_2^A = N_2^E$, such that $h(N_1^A - 1) = x_{max}$ and $h(N_2^A - 1) = y_{max}$. When the interface is flat and located at $x_3 = 0$, the number of grid points in the vertical direction satisfies $(N_3^A - 1)h = -z_{min}$ and $(N_3^E - 1)h = z_{max}$. When the interface is described by a surface $x_3 = \tau(x_1, x_2)$, the number of grid points in the vertical direction is chosen to make the average vertical grid spacing approximately the same as in the horizontal directions.

7.2 The method of manufactured solution

We start by verifying our implementation using the method of manufactured solution on a domain of size, $x_{max} = y_{max} = z_{max} = 10^4$, $z_{min} = -10^4$, and a flat interface at $x_3 = 0$. We define the manufactured solution to be

$$\mathbf{w}(x_1, x_2, x_3, t) = \begin{pmatrix} \sin(\omega(x_1 - ct))\sin(\omega x_2 + \phi)\sin(\omega x_3 + \phi) \\ \sin(\omega x_1 + \phi)\sin(\omega(x_2 - ct))\sin(\omega x_3 + \phi) \\ \sin(\omega x_1 + \phi)\sin(\omega x_2 + \phi)\sin(\omega(x_3 - ct)) \end{pmatrix},$$

in the elastic domain, and

$$\mathbf{q}(x_1, x_2, x_3, t) = \begin{pmatrix} 1 + 0.5\sin(\omega x_1)\cos(\omega x_2)\sin(\omega x_3)\sin(t + \phi) \\ \cos(\omega x_1 + \phi)\sin(\omega x_2)\cos(\omega x_3)\cos(2t) \\ \sin(\omega x_1)\sin(\omega x_2 + \phi)\sin(\omega x_3 + \phi)\cos(t + \phi) \\ \sin(\omega x_1)\cos(\omega x_2 + \phi)\cos(\omega x_3)\sin(3t) \\ 2 + \cos(\omega x_1)\sin(\omega x_2)\cos(\omega x_3)\sin(2t) \end{pmatrix},$$

in the atmospheric domain. In this test, we use the parameter values: $c = 1200$, $\omega = 2\pi \times 10^{-4}$, and $\phi = 0.17$. The material in the isotropic elastic domain is given the properties

$$\begin{aligned} \rho_e(x_1, x_2, x_3) &= A_r(2 + \sin(\omega_m x_1 + \phi_m)\cos(\omega_m x_2 + \phi_m)\sin(\omega_m x_3 + \phi_m)), \\ \mu(x_1, x_2, x_3) &= A_m(3 + \cos(\omega_m x_1 + \phi_m)\sin(\omega_m x_2 + \phi_m)\sin(\omega_m x_3 + \phi_m)), \\ \lambda(x_1, x_2, x_3) &= A_l(2 + \sin(\omega_m x_1 + \phi_m)\sin(\omega_m x_2 + \phi_m)\cos(\omega_m x_3 + \phi_m)), \end{aligned}$$

h	$\|\|Error\|\|_\infty$	$\|\|Error\|\|_2$	p_∞	p_2
100	4.34556e-6	1.23753e-6	–	–
50	2.60697e-7	7.33043e-8	4.06	4.08
25	1.62288e-8	4.45235e-9	4.01	4.04
12.5	9.26580e-10	2.74007e-10	4.13	4.02

Table 1: Method of manufactured solution errors in the elastic domain.

h	$\|\|Error^{(c)}\|\|_\infty$	$\|\|Error^{(c)}\|\|_2$	$p_\infty^{(c)}$	$p_2^{(c)}$	$\|\|Error^{(nc)}\|\|_\infty$	$\|\|Error^{(nc)}\|\|_2$	$p_\infty^{(nc)}$	$p_2^{(nc)}$
100	2.67239e-5	9.08813e-7	–	–	1.25382e-5	1.93939e-6	–	–
50	3.10750e-6	7.23756e-8	3.10	3.65	9.08927e-7	8.49688e-8	3.79	4.51
25	3.71912e-7	6.17450e-9	3.06	3.55	5.98950e-8	4.35040e-9	3.92	4.29
12.5	4.54034e-8	5.38631e-10	3.03	3.52	3.11309e-9	2.61771e-10	4.27	4.05

Table 2: Method of manufactured solution errors in the atmospheric domain. Boundary characteristic variables (superscript (c)) and non-boundary characteristic variables (superscript (nc)) are reported separately.

with parameters $A_r = 500$, $A_m = 83 \times 10^6$, $A_l = 83 \times 10^6$, $\omega_m = 2\pi \times 10^{-4}$, and $\phi_m = 0.2$. The background flow field in the atmospheric domain is defined to be

$$
\begin{aligned}
\hat{\rho}(x_1,x_2,x_3) &= 2 + \cos(\omega_m x_1)\sin(\omega_m x_2 + \phi_m)\sin(\omega_m x_3),\\
\hat{u}_1(x_1,x_2,x_3) &= \sin(\omega_m x_1)\cos(\omega_m x_2)\cos(\omega_m x_3),\\
\hat{u}_2(x_1,x_2,x_3) &= \cos(\omega_m x_1 + \phi_m)\sin(2\omega_m x_2)\cos(\omega_m x_3 + \phi_m),\\
\hat{u}_3(x_1,x_2,x_3) &= \cos(\omega_m x_1 + \phi_m)\cos(2\omega_m x_2 + \phi_m)\sin(\omega_m x_3),\\
\hat{c}(x_1,x_2,x_3) &= 330 + \sin(2\omega_m x_1)\cos(\omega_m x_2 + \phi_m)\sin(\omega_m x_3).
\end{aligned}
$$

Note that the background velocity has zero normal component at the interface, $\hat{u}_3(x_1,x_2,0) = 0$, as required by (3). The forcing functions $\mathbf{g}$ in (7) and $\mathbf{f}$ in (12) are constructed such that the solution equals the manufactured solution given the above material properties. The manufactured solutions are then used as initial data when numerically solving the elastic wave equation and the linearized Euler equations. The manufactured solution, the domain size, and the material properties have here been chosen to have sizes that are of the same order of magnitude as data used in realistic simulations.

The problem is solved to final time $T = 8$. One difficulty with the method of manufactured solution for the linearized Euler equations is that the zeroth order term ($H\mathbf{q}$ in (15)) can lead to bounded exponential growth of the error. Here, the final time is chosen small enough to prevent the error to be dominated by exponentially growing modes.

Before evaluating the solution error in the acoustic domain, we scale the pressure by $1/\hat{\rho}\hat{c}$ and the density by $\hat{c}/\hat{\rho}$, giving all components of the solution the dimension of velocity. The errors at the final time, measured in maximum and L_2 norm together with estimated convergence rates, are displayed in Tables 1–2. The observed convergence rate in the elastic domain is of order four in both norms, whereas in the atmospheric domain it appears that only a subset of the variables are fourth order accurate. These findings are consistent with our previous numerical results for a one-dimensional model of the coupled elastic-acoustic system [29].

One possible explanation for the lower convergence rate is the third order accurate difference operator used near the interface. The standard result for finite difference methods for hyperbolic PDEs, see [11], is that the accuracy in the solution will be one order higher than the order of the truncation error near the boundary. This result was proved under the assumption that the boundary is non-characteristic. In our case, that assumption would be satisfied if all eigenvalues of the matrix $\tilde{C}$ in the linearized Euler system (33) were non-zero. For a Cartesian grid, $\tilde{C} = C$. The matrix C is defined in (14) and has the eigenvalues $\hat{u}_3 \pm \hat{c}$, and $\hat{u}_3$ (with multiplicity three). Unfortunately, the zero normal velocity condition (3) implies that $\hat{u}_3 = 0$ along $x_3 = 0$, which means that three eigenvalues of C are zero on the interface. Hence, the assumption of a non-characteristic boundary is violated, and

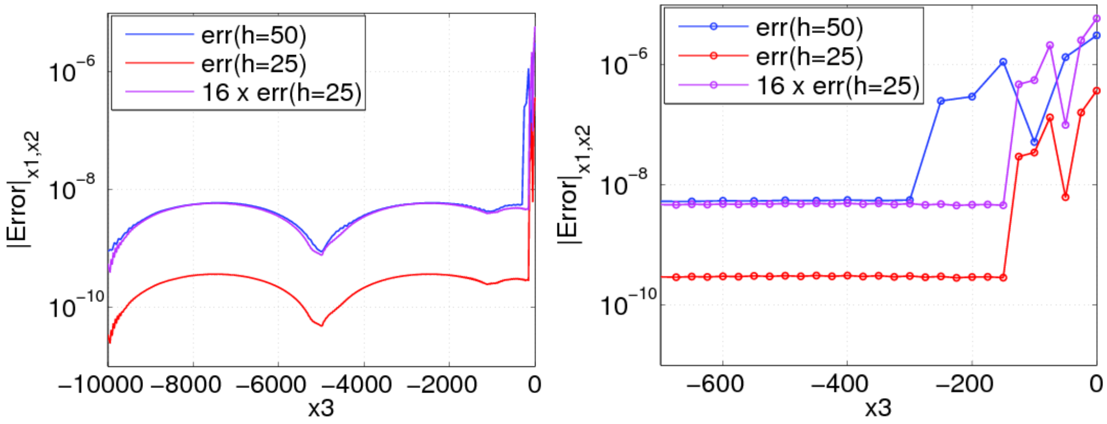

Figure 3: Maximum norm error in the boundary characteristic variable (87) over (x_1, x_2) as function of x_3, at time $T = 8$. The left sub-plot shows a close-up near $x_3 = 0$, where the error at each grid point is marked by a circle. Blue lines correspond to the coarse grid ($h = 50$), red is the fine grid ($h = 25$), and magenta shows $16\times$ the $h = 25$ error (fourth order convergence rate occurs where the magenta and blue curves coincide).

the theory in [11] does not directly apply.

In order to analyze the error in the atmospheric domain in more detail, we decompose the solution into two parts. The first part consists of the boundary characteristic components, corresponding to the zero eigenvalues of C, i.e., u_1, u_2, and

$$\frac{\hat{c}}{\hat{\rho}}\rho - \frac{1}{\hat{c}\hat{\rho}}p. \tag{87}$$

The error in these variables is denoted by superscript (c) in Table 2. The second part of the solution consists of the remaining (non-boundary characteristic) components of the solution, i.e., u_3 and the scaled pressure,

$$\frac{1}{\hat{c}\hat{\rho}}p. \tag{88}$$

The errors in these variables is denoted by superscript (nc) in Table 2. It can be seen that the solution in the non-boundary characteristic variables is fourth order accurate in both norms. However, the boundary characteristic variables are only third order accurate in maximum norm, and converge with order 3.5 in L_2.

A further inspection of the error in the atmospheric domain is presented in Figures 3 and 4, where we evaluate the max-norm of the error over the x_1- and x_2-directions for each grid plane $x_3 = x_{3,k}$,

$$|Error|_{x_1,x_2}(x_{3,k}) = max_{i,j}|Error_{i,j,k}|.$$

The error near $x_3 = 0$ behaves noticeably different for boundary and non-boundary characteristic components of the solution. The behavior of the boundary characteristic components is exemplified by the variable (87) in Figure 3. Note that the error is significantly smaller in the interior than near the interface at $x_3 = 0$. The close up in Figure 3 clearly shows that the error is the largest at the first six grid points, where it is a non-smooth function of x_3. These six grid points coincide exactly with where the summation by parts operator is third order accurate. Because the variable (87) corresponds to a zero eigenvalue of the matrix C, the corresponding error can not propagate in the x_3-direction. In other words, the error is trapped along the interface. This explains the observed third order convergence in max norm. The convergence is faster in the L_2 norm because the error is only large at a fixed number of grid points next to the interface.

The error behavior for a non-boundary characteristic solution component is demonstrated by the u_3-variable, see Figure 4. This variable corresponds to a non-zero eigenvalue of C, which means that the corresponding error propagates into the domain, away from the interface. Even though the error is non-smooth near the interface, the accuracy of this component of the solution follows the theory in [11] and converges with fourth order accuracy.

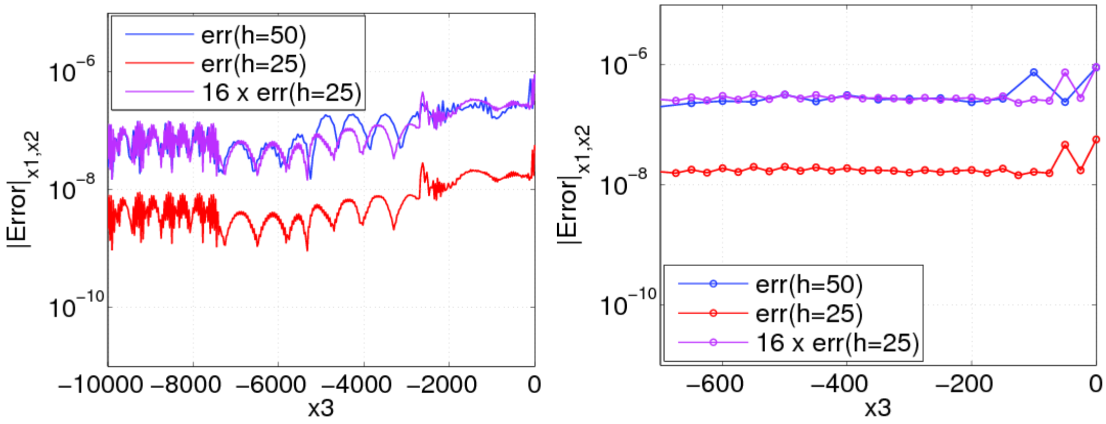

Figure 4: Maximum norm error in the non-boundary characteristic variable u_3 over (x_1, x_2) as function of x_3, at time $T = 8$ (left). The right plot shows a close-up near $x_3 = 0$. The colors are the same as in Figure 3.

7.3 Acoustic point source

If the background flow velocity in the atmospheric domain is zero and the speed of sound is constant, the pressure perturbation due to a point source satisfies the scalar wave equation

$$p_{tt} = \hat{c}^2 \nabla \cdot \nabla p + f_t(\mathbf{x}, t), \quad f(\mathbf{x}, t) = f_0\, g(t)\, \delta(\mathbf{x} - \mathbf{x}_0), \tag{89}$$

where $\mathbf{x}_0 = (x_0, y_0, z_0)$ is the position of the source, f_0 is its amplitude, and $g(t)$ is a smooth time function, which we take to be the Gaussian

$$g(t) = \frac{\omega}{\sqrt{2\pi}} e^{-\omega^2 (t-t_0)^2/2}, \quad t_0 = 1.8\text{s}, \quad \omega = 3.5\text{rad/s}. \tag{90}$$

This problem has an analytical solution, which can be used to evaluate the accuracy of the pressure in the numerical solution of the linearized Euler equations. In this test, we solve the linearized Euler equations in the half-space $x_3 \le 0$ with a constant background flow field with zero velocity. During this test, the elastic simulation is disabled, and the interface condition (79) is replaced by the solid wall boundary condition $u_3 = 0$ on $x_3 = 0$. All other boundaries have super-grid layers.

A mirroring technique is used to obtain the analytical solution of the half-space problem as the sum of two whole-space solutions of (89). The resulting analytical solution is

$$p(\mathbf{x}, t) = \frac{f_0}{4\pi \hat{c}^2} \left[g'(t - |\mathbf{x} - \mathbf{x}_0|/\hat{c}) + g'(t - |\mathbf{x} - \mathbf{x}_m|/\hat{c}) \right],$$

where the mirror image source is located at $\mathbf{x}_m = (x_0, y_0, -z_0)$.

In the symmetrized linearized Euler equations (15), the point source corresponds to the forcing term

$$\mathbf{f} = \frac{f(\mathbf{x}, t)}{\sqrt{\gamma} \hat{p} \hat{c}} \begin{pmatrix} 1 & 0 & 0 & 0 & \sqrt{\gamma - 1} \end{pmatrix}^T. \tag{91}$$

We use the technique described in [22] to discretize the singular point source in space. In the numerical simulation, we take the background pressure to be $\hat{p} = 1.025 \times 10^5$ Pa and the speed of sound is set to $\hat{c} = 331$ m/s. The computational domain has size $x_{max} = 5000$ m, $y_{max} = 5000$ m, $z_{min} = -5000$ m, with the source located at $\mathbf{x}_0 = (2504, 2010, -50)m$. The amplitude of the point source is set to $f_0 = 1.0 \times 10^5$ J.

Figure 5 (left) shows the numerical pressure vs. time at the location $\mathbf{x}_r = (1500, 2000, -1500)$ m in red color, together with the analytical solution plotted in black color, giving almost indistinguishable results. The computation used 201^3 grid points, corresponding to grid spacing $h = 25$. In Figure 5 (right) we show the error at the

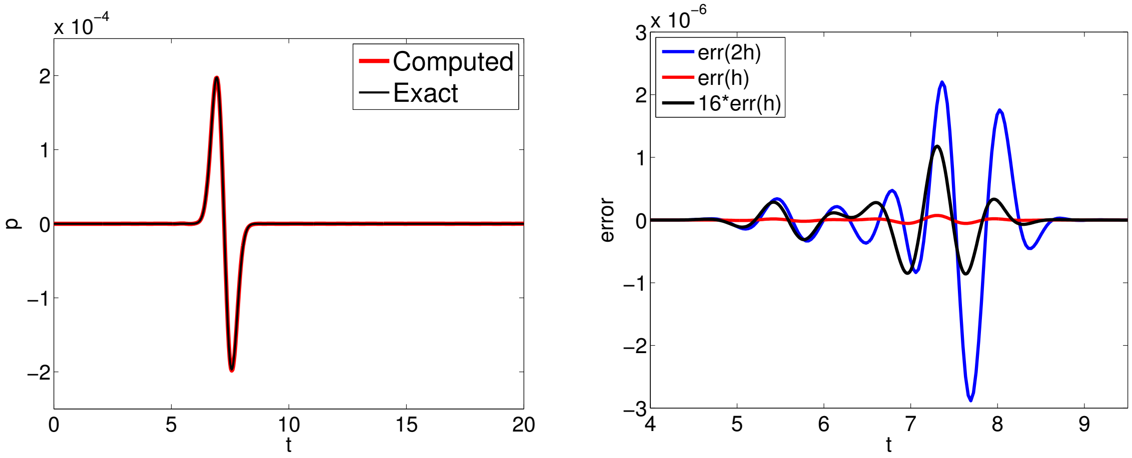

Figure 5: Acoustic point source in a half space. Left: Pressure vs. time for exact (black) and computed (red) solutions obtained with 201^3 grid points. Right: Close-up of error in pressure vs. time for two grid sizes (201^3 grid points in blue; error with 401^3 grid points in red); 16 × the error on the fine grid in black.

same station obtained on two different grids. The coarse grid has 201^3 grid points and the fine grid has 401^3 grid points. The coarse grid error is plotted in blue color, and the fine grid error in red color. Figure 5 (right) shows that up to time 7, the error is reduced by a factor that is close to 16 when the grid spacing is refined by a factor 2, corresponding to perfect fourth order convergence. The observed convergence rate is even better than fourth order towards the later times. The effect of the characteristic boundary at $x_3 = 0$ does not appear to propagate into the domain.

The Gaussian source time function (90) has center frequency $f_0 = 0.56$ Hz and a highest significant frequency of $f_{max} \approx 1.39$ Hz, corresponding to the shortest significant wave length $\lambda_a = \hat{c}/f_{max} \approx 238$ m. Thus, the grid sizes $h = 25$ m and $h = 12.5$ m correspond to 9.5 and 19 grid points per wave length, respectively. Since the numerical solutions on the two grids are close to indistinguishable, we conclude that 9.5 grid points per wave length provides very good accuracy for this problem.

7.4 Coupled wave propagation due to a point source

To further investigate the accuracy of the proposed method, we study coupled wave propagation due to a point source in either the acoustic, or in the elastic domain. The configuration is outlined in Figure 6. We take the interface to be the plane $x_3 = 0$ and let the computational domain be a box with $x_{max} = y_{max} = 4,000$ m, $z_{max} = 1,500$ m, and $z_{min} = -1,500$ m. We consider a calm atmosphere with constant temperature $\hat{T} = 272.95$ K and pressure $\hat{p} = 1.025 \cdot 10^5$ Pa, corresponding to the speed of sound $\hat{c} = 331$ m/s and density $\hat{\rho} = 1.31$ kg/m^3. The solid earth is modeled by an isotropic elastic material with density $\rho_e = 1,500$ kg/m^3, compressional velocity $V_p = 1,000$ m/s, and shear velocity $V_s = 500$ m/s. The numerical solutions are recorded at three receiver locations:

$$\mathbf{x}_a = (3,3,-0.5) \cdot 10^3 \text{ m}, \quad \mathbf{x}_i = (3,3,0) \cdot 10^3 \text{ m}, \quad \mathbf{x}_e = (3,3,0.5) \cdot 10^3 \text{ m}.$$

When the forcing is in the acoustic domain, we use a point source of the form (91) with the Gaussian time function (90). In this case, we locate the source at $\mathbf{x}_{0a} = (2,2,-0.5) \cdot 10^3$ m, and set the source amplitude to $f_0 = 10^{10}$ J. Furthermore, we set $\omega = 6.283$ rad/s and $t_0 = 0.96$ s in the Gaussian time function. This problem is difficult to solve analytically, and we use the numerical solution on a fine grid to approximate the exact solution. For the acoustic source we focus on the ground motions at two locations in the elastic domain; on the interface (at $\mathbf{x}_i$), and in the interior (at $\mathbf{x}_e$), see Figure 7. To investigate how the accuracy in the solution depends on the grid size, we repeat the simulation with four grid sizes: $h = \{40,20,10,5\}$. The solution on the $h = 5$ grid is used as reference solution. Let $w_q^{(h)}(t)$ denote the qth displacement component of the numerical solution with grid size h.

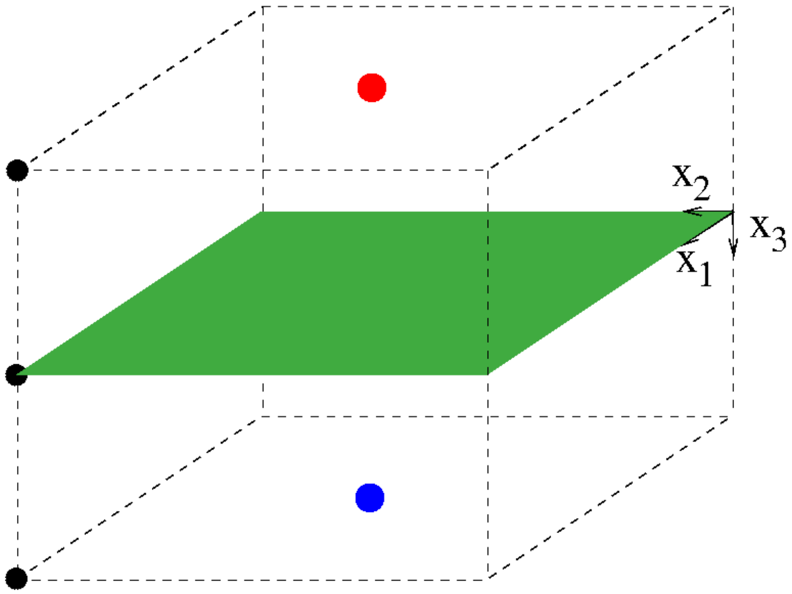

Figure 6: The problem setup for coupled wave propagation due to a point source in either the acoustic domain (red circle), or in the elastic domain (blue circle). The green plane marks the interface, and the three black circles indicate the receiver stations.

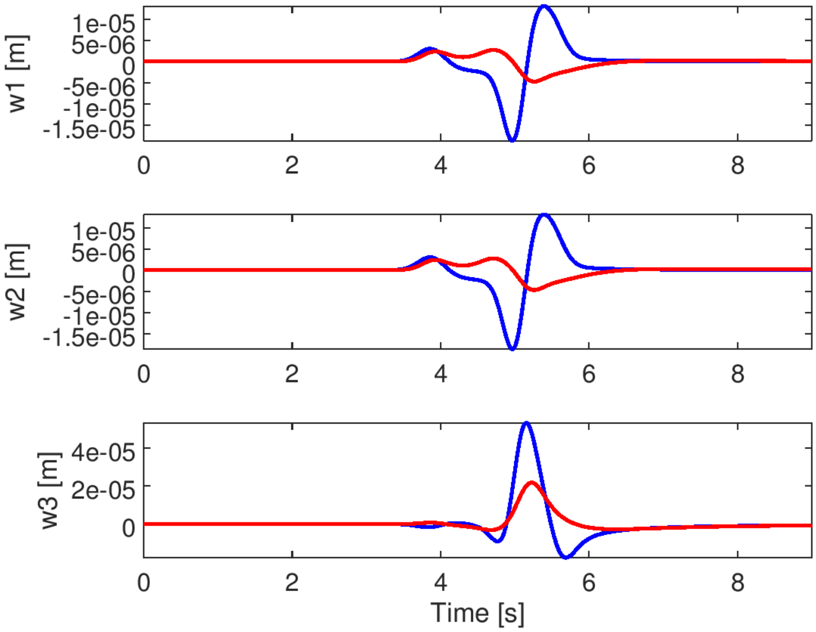

Figure 7: The elastic response due to a point source in the acoustic domain. The blue lines show the displacement at $\mathbf{x}_i$ (on the interface), and the red lines show the displacement at $\mathbf{x}_e$ (in the interior).

h	P	$\|\Delta w^{(h)}\|(\mathbf{x}_i)$	ratio	$\|\Delta w^{(h)}\|(\mathbf{x}_e)$	ratio
40	3.3	1.18e-1	–	1.10e-1	–
20	6.6	1.27e-2	9.29	3.76e-3	29.26
10	13.2	9.70e-4	13.09	1.60e-4	23.50
5	26.5	0	–	0	–

Table 3: Point source in the acoustic domain. Relative norm of difference in the displacement components as function of the grid size (h) and grid points per wave length (P), relative to the reference solution ($h = 5$). The locations $\mathbf{x}_i$ and $\mathbf{x}_e$ are on the interface and in the interior of the elastic domain, respectively.

We define the norm of the relative difference from the reference solution by

$$\|\Delta w^{(h)}\| = \frac{\max_t \sqrt{\sum_{q=1}^{3}(w_q^{(h)}(t) - w_q^{(5)}(t))^2}}{\max_t \sqrt{\sum_{q=1}^{3}(w_q^{(5)}(t))^2}}. \tag{92}$$

This norm is evaluated at the receiver locations $\mathbf{x}_i$ and $\mathbf{x}_e$, see Table 3. We note that the differences are slightly larger at the receiver on the interface than in the interior of the domain. If the grid sizes are small enough and the numerical solution is fourth order accurate, we would expect the convergence ratio $\|\Delta w^{(20)}\|/\|\Delta w^{(10)}\| = 17$. The observed convergence ratio is slightly lower on the interface, while it is higher than expected in the interior. Of more practical value is to evaluate the differences as function of the number of grid points per smallest wave length,

$$P = \frac{\hat{c}_{min}}{h f_{max}}. \tag{93}$$

The parameters in the Gaussian time function correspond to the dominant frequency $f_0 = \omega/(2\pi) \approx 1$ Hz and we estimate the highest significant frequency by $f_{max} \approx 2.5$ Hz. The smallest phase velocity occurs in the acoustic domain, with $\hat{c}_{min} = 331$ m/s. The grid size in the reference solution corresponds to $P = 26.5$ points per wave length, indicating that it is well resolved on the mesh. The results in Table 3 indicate that $P = 6.6$ gives adequate resolution ($\approx 1\%$ error) for this problem.

When the forcing is in the elastic domain, we use a point moment tensor source defined by

$$\mathbf{g}(\mathbf{x},t) = g(t) M_0 \begin{pmatrix} 0.5 & 1 & 0 \\ 1 & 0.5 & 0 \\ 0 & 0 & 0.5 \end{pmatrix} \nabla\delta(\mathbf{x} - \mathbf{x}_{0e}), \quad M_0 = 10^{15} \text{ Nm}, \tag{94}$$

located at $\mathbf{x}_{0e} = (2, 2, 0.5) \cdot 10^3$ m. Here, $\nabla\delta$ is the gradient of the Dirac distribution, which is discretized in space by using the technique described in [23]. This type of source function is often used to model small earthquakes. Because the symmetric matrix in (94) has diagonal and off-diagonal elements, the source will generate both compressional and shear waves. In addition, surface waves are triggered when the main wave front is reflected by the interface. In this test we use the same Gaussian source time function and the same grid sizes as for the acoustic source. We focus on the acoustic response on the interface (at $\mathbf{x}_i$) and in the interior (at $\mathbf{x}_a$). Figure 8 shows the numerical reference solution ($h = 5$) at these locations.

To construct a dimensionally consistent norm of the numerical solution in the acoustic domain, we define the scaled density and pressure,

$$\tilde{\rho} = \rho\hat{c}/\hat{\rho}, \quad \tilde{p} = p/\hat{\rho}\hat{c},$$

and denote the scaled solution $\mathbf{v} = (\tilde{\rho}, u_1, u_2, u_3, \tilde{p})^T$. As a result, all components of $\mathbf{v}$ have the dimension of velocity and approximately the same amplitude. The norm of the relative difference between the numerical solutions follows by generalizing (92) to sum over the 5 components of $\mathbf{v}$.

The numerical simulation is performed for each grid size, and the norm of the relative difference is evaluated at the receiver locations $\mathbf{x}_i$ and $\mathbf{x}_a$, see Table 4. We note that the values of $\|\mathbf{v}^{(h)}\|$ are slightly higher compared to

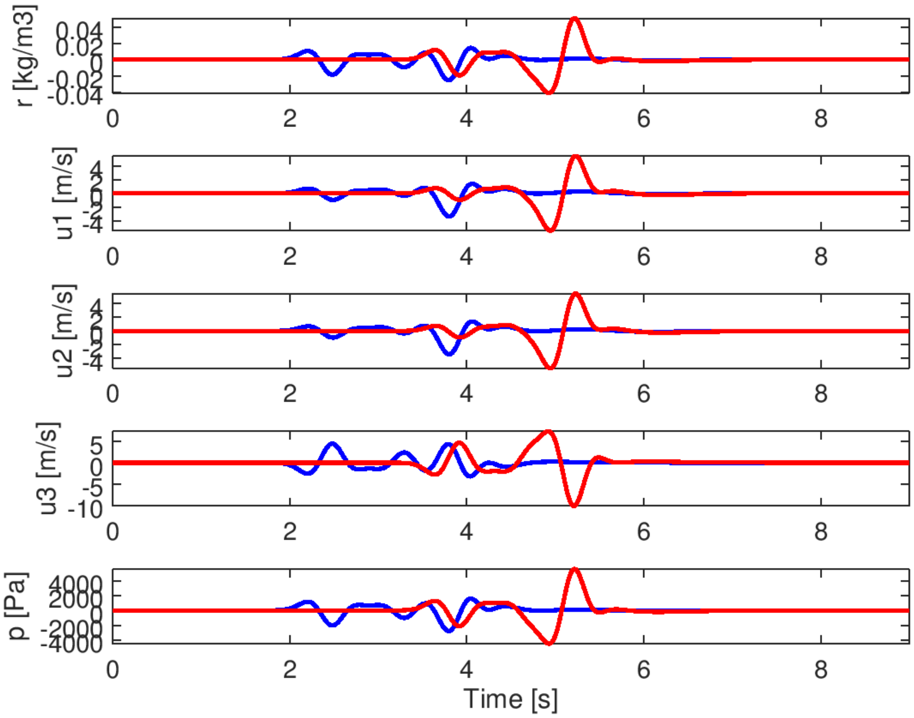

Figure 8: The acoustic response due to a point source in the elastic domain. From top to bottom, the solution components are the density (ρ), the velocity components (u_1, u_2, u_3), and the pressure (p). The blue lines show the solution at $\mathbf{x}_i$ (on the interface), and the red lines show the solution at $\mathbf{x}_a$ (in the interior).

h	P	$\|\Delta v^{(h)}\|(\mathbf{x}_i)$	ratio	$\|\Delta v^{(h)}\|(\mathbf{x}_a)$	ratio
40	3.3	1.05e-1	–	3.29e-1	–
20	6.6	2.88e-2	3.64	7.68e-2	4.28
10	13.2	1.87e-3	15.40	4.42e-3	17.37
5	26.5	0	–	0	–

Table 4: Point source in the elastic domain. Relative norm of difference in scaled acoustic response, as function of the grid size (h) and grid points per wave length (P), relative to the reference solution ($h = 5$). The locations $\mathbf{x}_i$ and $\mathbf{x}_a$ are on the interface and in the interior of the acoustic domain, respectively.

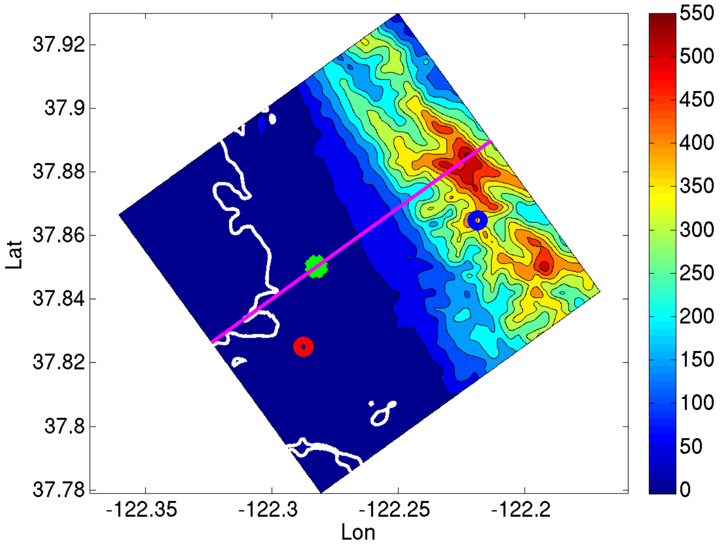

Figure 9: Elevation of the topography (in meters) near Berkeley, CA. The white line indicates the shore line and the magenta line indicates the vertical cross-section where the solution is saved. The horizontal projection of the source location is marked in green; the red and blue circles mark the observation stations.

the displacements in Table 3. As in the previous case, the ratio between the norm of the differences for $h = 20$ and $h = 10$ should be 17 if the solution is perfectly forth order accurate. The observed ratio is close to that number for both locations. In this case, the acoustic waves have a more complex waveform than in the previous example. From the results in Table 3, we see that the max norm difference from the reference solution is close to 8 % for $P = 6.6$ points per wave length, indicating that a finer mesh should be used to obtain an accurate numerical solution.

7.5 Coupled wave propagation in a realistic windy atmosphere and a heterogeneous elastic model

To demonstrate the full capabilities of the proposed method, we simulate the wave propagation from a fictitious bolide burst near Berkeley, CA. The computational domain is 12 km by 12 km in the horizontal directions, extends 5 km into the earth, and 7 km into the atmosphere. The topography is shown in Figure 9. In geographical coordinates, the origin of the computational domain is located at longitude -122.25 degrees and latitude 37.93 degrees. The x_1-direction is rotated clockwise by 143.638 degrees from the north.

The atmosphere has a temperature that decreases linearly from 288 K at the surface to 236 K at 8 km altitude, with a horizontal wind directed from the south. The density and speed of sound of the background field follow from the ideal gas law,

$$\hat{p} = \hat{\rho}\frac{R}{M}\hat{T}, \quad \hat{c}^2 = \frac{\gamma R \hat{T}}{M}, \tag{95}$$

where (in SI-units), $M = 0.029$, $R = 8.3145$, and $\gamma = 1.4$. The ideal gas law gives a density profile for each data point in Table 5. It is straightforward to verify that this profile is in approximate gravitational balance with the pressure profile, see Appendix A for details. Linear interpolation of the data points in Table 5 is used to specify the background flow field at intermediate altitudes. The topographic elevation and the isotropic material properties of the elastic domain are obtained from the USGS model of the San Francisco bay area [6].

We model the fictitious bolide burst by a point source of the form (91) located at $x_1 = 5500$ m, $x_2 = 7500$ m, at an altitude of 1000 m (green marker in Figure 9). We set the source amplitude to $f_0 = 1.0 \times 10^{11}$ J, and use a Gaussian source time function with $\omega = 3.5$ rad/s, corresponding to the center frequency 0.56 Hz and a highest significant frequency of $f_{max} = 1.39$ Hz.

Altitude (km)	Temperature (K)	Pressure (Pa)	Wind speed (m/s)
0	288.1	1.013×10^5	0
2	275.2	7.950×10^4	1.77
4	262.2	6.166×10^4	3.37
6	249.2	4.722×10^4	4.22
8	236.2	3.565×10^4	4.21

Table 5: Data points determining the atmosphere for the simulation.

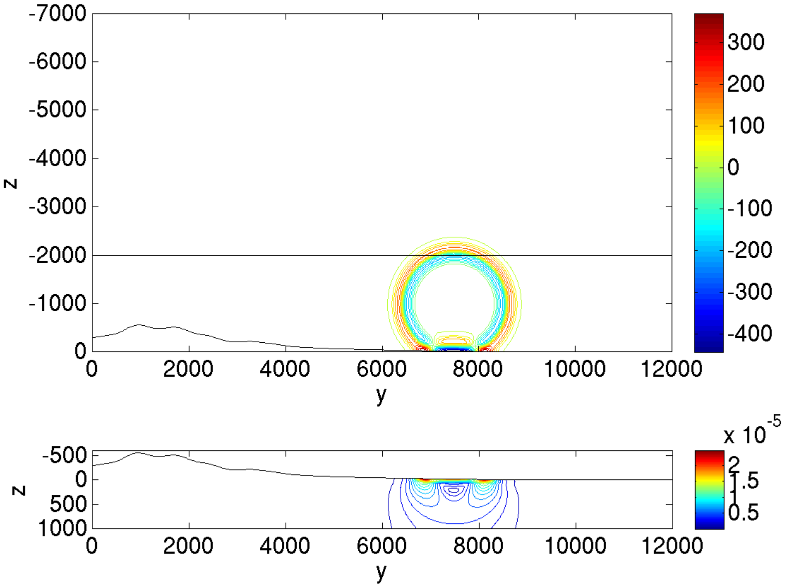

Figure 10: Pressure perturbation [Pa] (top) and displacement magnitude [m] (bottom) along the plane $x_1 = 5500$ m, at time $t = 5$ s.

The lowest shear speed in the elastic material is 500 m/s and the minimum speed of sound in the atmosphere is 312 m/s. We model the wave propagation on a grid with spacing $h = 20$ m, corresponding to 11.2 grid points per shortest wave length. The computational grid has a total of 218 million points and the simulation was run to time $t = 20$ s, corresponding to 15,376 time steps.

Figure 10 and 11 display the pressure perturbation and displacement magnitude on a vertical cross-section through the source ($x_1 = 5500$ m), at times $t = 5$ s and $t = 11$ s, respectively. Here the direct and reflected acoustic waves are clearly visible. In the elastic domain, the motion is the strongest near the surface, where the acoustic pressure wave is reflected by the topography. For this reason, we only show a thin layer of the elastic domain near the surface. Small amplitude elastic waves are triggered by the impact of the acoustic wave. These waves propagate significantly faster than the acoustic waves, as is visible in Figure 11.

We record the time-histories of the solution at two stations on the surface. The first station is located near the shore line, south-west of the source, at $(x, y) = (7500, 9500)$ m (red circle in Figure 9). The second station is located in the hills, north-east of the source, at $(x_1, x_2) = (7500, 2000)$ m (blue circle in Figure 9). The recorded pressure perturbations are shown in Figure 12. The corresponding displacement magnitudes are shown in Figure 13. Note that the primary acoustic wave first reaches the topography at $t \approx 4$ s, generating head waves in the elastic domain that propagate much faster than the speed of sound in the atmosphere. This explains why the elastic waves reach the observation stations before the acoustic waves. Also note that the displacement at the North-East station is significantly smaller than at the South-West station. This is due to geometric spreading of the pressure wave as well as different material properties at the two stations, with the South-West station in a soft sedimentary basin and

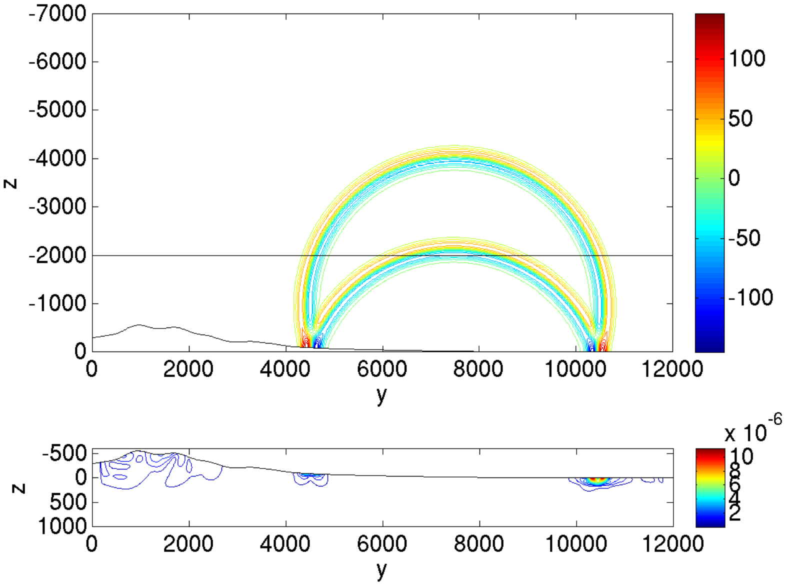

Figure 11: Pressure perturbation [Pa] (top) and displacement magnitude [m] (bottom) along the plane $x_1 = 5500$ m, at time $t = 11$ s.

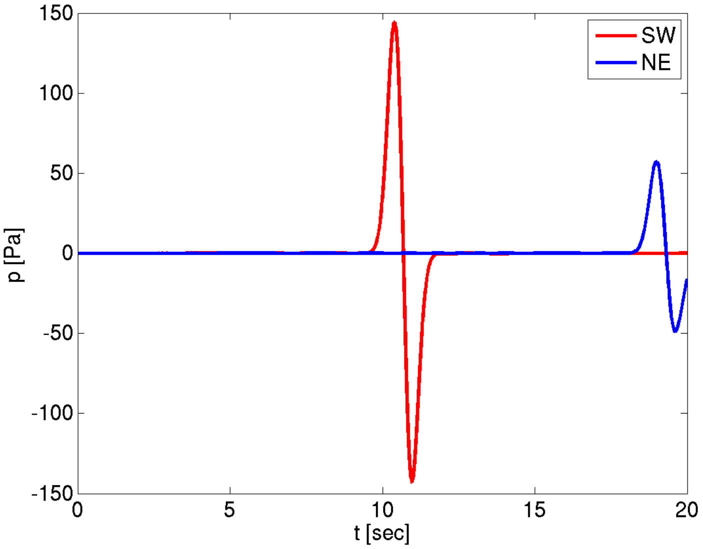

Figure 12: Time history of the pressure perturbation [Pa] at the South-West (red) and the North-East (blue) stations.

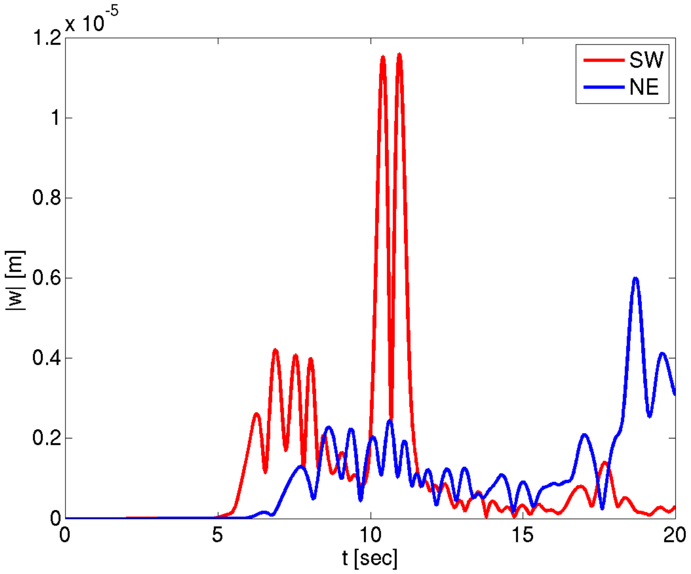

Figure 13: Time history of the displacement magnitude [m] at the South-West (red) and the North-East (blue) stations.

the North-East station on hard rock.

To illustrate the quality of the super-grid far field closure, we plot the pressure perturbation and displacement magnitude at time $t = 20$ s, see Figure 14. In this calculation, the super-grid layers are 30 grid points thick, corresponding to 600 meters in physical coordinates. The plot shows a cross-section of the entire computational domain, and the solution has no physical meaning within the layers, which extend 600 meters from the outer boundary. At $t = 20$ s, the primary pressure wave has entered the super-grid layer along the top boundary, and both the primary and reflected pressure wave have entered the layer on the right side. In the elastic domain, waves have entered the super-grid layers on both the left and right sides. We conclude that the super-grid layers are performing very well, as no artificial reflections are visible in these plots.

8 Conclusions

We have presented a high order accurate finite difference method for simulating the coupled motion of acoustic and seismic wave propagation. Our acoustic model captures wave propagation in a moving atmosphere, described by an ideal perfect gas. For seismic exploration applications, it would be interesting to generalize the acoustic model to capture wave propagation in water. Furthermore, to accurately propagate seismic signals over long distances, it would also be appropriate to include effects of visco-elastic attenuation in the solid earth, e.g. by following the approach in [24].

Because the wave speeds in the solid earth often are higher than in the atmosphere, it would be desirable to generalize the discretization to use different grid sizes in the two domains, resulting in a mesh with hanging nodes along the interface. We believe the conservative interpolation technique for the elastic wave equation by Petersson and Sjogreen [23] could be generalized to give an energy conserving discretization for the coupled seismo-acoustic problem. Another desirable generalization would be to allow for different time steps in the acoustic and elastic sub-domains.

Acknowledgements

We thank Prof. E. Dunham at Stanford University for interesting discussions on atmospheric flows. This work was performed under the auspices of the U.S. Department of Energy by Lawrence Livermore National Laboratory

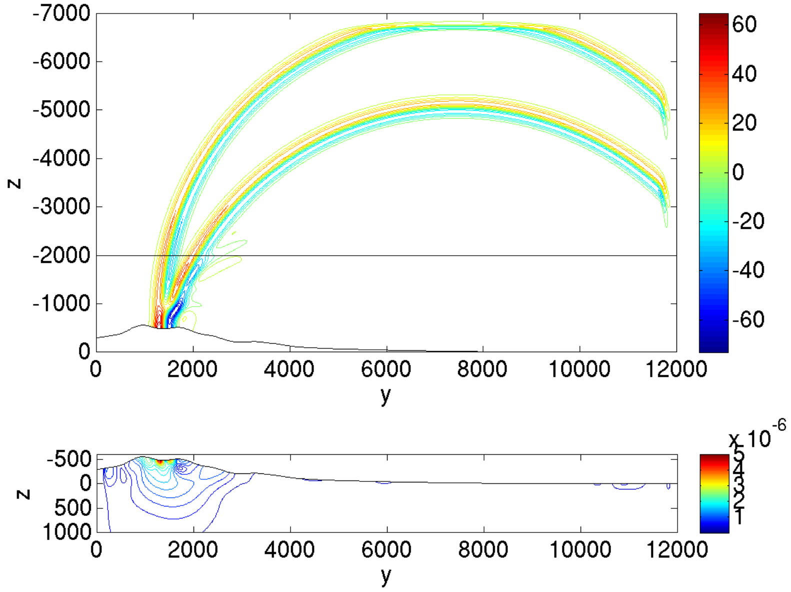

Figure 14: Pressure perturbation [Pa] (top) and displacement magnitude [m] (bottom) along the plane $x_1 = 5500$ m, at time $t = 20$ s The super-grid layers extend 600 m into the domain from the outer boundaries.

under contract DE-AC52-07NA27344. This is contribution LLNL-JRNL-704612.

A The background flow field

In general it is hard to derive exact solutions to the non-linear Euler equations. However, there are special cases where an exact solution is readily available. A constant background field is the simplest example. We will here consider a background field that only depends on the altitude and has no vertical wind component,

$$\hat{u}_1 = \hat{u}_1(x_3), \quad \hat{u}_2 = \hat{u}_2(x_3), \quad \hat{u}_3 = 0, \quad \hat{\rho} = \hat{\rho}(x_3), \quad \hat{p} = \hat{p}(x_3). \tag{96}$$

The field (96) satisfies the zero normal velocity condition (3) if the interface is flat. To satisfy the vertical momentum equation, the pressure is required to be in balance with gravity,

$$\frac{d\hat{p}}{dx_3} = g\hat{\rho}, \tag{97}$$

where g is the gravitational constant (x_3 is positive downwards). It is straightforward to verify that this background field is a solution of the non-linear Euler equations.

To analyze the gravitational potential energy P_g in (21), we write the ideal gas law (95) on the form $\hat{\rho} = \gamma\hat{p}/\hat{c}^2$. This and (97) give

$$\frac{d\hat{\rho}}{dx_3} = \frac{d\hat{\rho}}{d\hat{p}}\frac{d\hat{p}}{dx_3} = \frac{\gamma}{\hat{c}^2}g\hat{\rho}.$$

The definition of the Brunt-Väisälä frequency in (21) gives

$$\mathcal{N}^2 = -g\left(-\frac{1}{\hat{\rho}}\frac{d\hat{\rho}}{dx_3} + \frac{g}{\hat{c}^2}\right) = -g\left(-\frac{\gamma g}{\hat{c}^2} + \frac{g}{\hat{c}^2}\right) = (\gamma - 1)\frac{g^2}{\hat{c}^2}.$$

Substituting the expression for $\mathcal{N}^2$ into P_g in (21) and comparing to (20) shows that $P_g = P_2$.

References

[1] Abarbanel, S., Gottlieb, D.: Optimal time splitting for two- and three-dimensional Navier-Stokes equations with mixed derivatives. J. Comput. Phys. **41**, 1–33 (1981)

[2] Appelö, D., Colonius, T.: A high order super-grid-scale absorbing layer and its application to linear hyperbolic systems. J. Comput. Phys. **228**, 4200–4217 (2009)

[3] Appelö, D., Petersson, N.A.: A stable finite difference method for the elastic wave equation on complex geometries with free surfaces. Comm. Comput. Phys. **5**, 84–107 (2009)

[4] Arrowsmith, S.J., Johnson, J.B., Drob, D.P., Hedlin, M.A.H.: The seismoacoustic wavefield: A new paradigm in studying geophysical phenomena. Rev. Geophys. **48**, RG4003 (2010)

[5] Banks, J.W., Sjögreen, B.: Stability of numerical interface conditions for fluid/structure interaction. Commun. Comput. Phys. **10**, 279–304 (2011)

[6] Brocher, T.M.: Compressional and shear wave velocity versus depth in the San Francisco bay area, California: Rules for USGS bay area velocity model 05.0.0. Tech. rep., USGS Open-File Report 2005-1317 (2005)

[7] Carcione, J.M.: Wave fields in real media: wave propagation in anisotropic, anelastic and porous media, *Handbook of geophysical exploration: seismic exploration*, vol. 31. Pergamon, Elsevier Science (2001)

[8] Duru, K., Virta, K.: Stable and high order accurate difference methods for the elastic wave equation in discontinuous media. J. Comput. Phys. **279**, 37–62 (2014)

[9] Gill, A.: Atmosphere-Ocean Dynamics. Academic Press (1982)

[10] de Groot-Hedlin, C., Hedlin, M., Walker, K.: Finite difference synthesis of infrasound propagation through a windy, viscous atmosphere: application to a bolide explosion detected by seismic networks. Geophys. J. Int. **185**, 305–320 (2011)

[11] Gustafsson, B.: The convergence rate for difference approximations to mixed initial boundary value problems. Math. Comput. **29**(130), 396–406 (1975)

[12] Kreiss, H.O., Lorenz, J.: Initial-Boundary Value Problems and the Navier-Stokes Equations. Academic Press (1989)

[13] Kreiss, H.O., Scherer, G.: Finite element and finite difference methods for hyperbolic partial differential equations. In: Mathematical aspects of Finite Elements in Partial differential equations. Academic Press (1974)

[14] Landau, L.D., Lifshitz, E.M.: Fluid mechanics, vol. 6, 2nd edition edn. Butterworth-Heinemann (1959)

[15] Mattsson, K.: Summation by parts operators for finite difference approximations of second-derivatives with variable coefficients. J. Sci. Comput. **51**, 650–682 (2012)

[16] Mattsson, K., Nordström, J.: Summation by parts operators for finite difference approximations of second derivatives. J. Comput. Phys. **199**, 503–540 (2004)

[17] Munz, C.D., Dumbser, M., Roller, S.: Linearized acoustic perturbation equations for low mach number flow with variable density and temperature. J. Comput. Phys. **224**, 352–364 (2007)

[18] Nilsson, S., Petersson, N.A., Sjögreen, B., Kreiss, H.O.: Stable difference approximations for the elastic wave equation in second order formulation. SIAM J. Numer. Anal. **45**, 1902–1936 (2007)

[19] Olsson, P.: Summation by parts, projections, and stability. I. Math. Comput. **64**, 1035–1065 (1995)

[20] Olsson, P.: Summation by parts, projections, and stability. II. Math. Comput. **64**, 1473–1493 (1995)

[21] Ostashev, V.E., Wilson, D.K., Liu, L., Aldrigde, D.F., Symons, N.P., Marlin, D.: Equations for finite-difference, time-domain simulation of sound propagation in moving inhomogeneous media and numerical implementation. J. Acoust. Soc. Am. **117**(2), 503–517 (2005)

[22] Petersson, N.A., O'Reilly, O., Sjögreen, B., Bydlon, S.: Discretizing singular point sources in hyperbolic wave propagation problems. J. Comput. Phys. **321**, 532–555 (2016)

[23] Petersson, N.A., Sjögreen, B.: Stable grid refinement and singular source discretization for seismic wave simulations. Commun. Comput. Phys. **8**, 1074–1110 (2010)

[24] Petersson, N.A., Sjögreen, B.: Stable and efficient modeling of anelastic attenuation in seismic wave propagation. Comm. Comput. Phys. **12**(1), 193–225 (2012)

[25] Petersson, N.A., Sjögreen, B.: Super-grid modeling of the elastic wave equation in semi-bounded domains. Commun. Comput. Phys. **16**, 913–955 (2014)

[26] Petersson, N.A., Sjögreen, B.: User's guide to SW4, version 1.1. Tech. Rep. LLNL-SM-662014, Lawrence Livermore National Laboratory (2014). (Source code available from `geodynamics.org/cig`)

[27] Petersson, N.A., Sjögreen, B.: Wave propagation in anisotropic elastic materials and curvilinear coordinates using a summation-by-parts finite difference method. J. Comput. Phys. **299**, 820–841 (2015)

[28] Sjögreen, B., Petersson, N.A.: A fourth order accurate finite difference scheme for the elastic wave equation in second order formulation. J. Scient. Comput. **52**, 17–48 (2012)

[29] Sjögreen, B., Petersson, N.A.: Summation by parts finite difference approximations for seismic and seismo-acoustic computations. In: J.S.H. R. M. Kirby M. Berzins (ed.) Spectral and High Order Methods for Partial Differential Equations, *Lecture Notes in Computational Science and Engineering*, vol. 106, pp. 455–463. Springer Verlag (2015)

[30] Sjögreen, B., Petersson, N.A.: User's guide to ElAc, version 1.0. Tech. Rep. LLNL-SM-704300, Lawrence Livermore National Laboratory (2016)

[31] Strand, B.: Summation by parts for finite difference approximations for d/dx. J. Comput. Phys. **110**, 47–67 (1994)

[32] Svard, M., Nordstrom, J.: On the order of accuracy for difference approximations of initial-boundary value problems. J. Comput. Phys. **218**, 333–352 (2006)

[33] Thompson, J.F., Warsi, Z.U.A., Mastin, C.W.: Numerical grid generation: foundations and applications. Elsevier North-Holland, Inc., New York, NY, USA (1985)

[34] Tromp, J., Komatitsch, D., Liu, Q.: Spectral-element and adjoint methods in seismology. Commun. Comput. Phys. **3**(1–32) (2008)

[35] Virieux, J.: P-SV wave propagation in heterogeneous media: Velocity-stress finite-difference method. Geophysics **51**(4), 889–901 (1986)